Insights Into the Electronic Structure of Cu^{II} Bound to an Imidazole Analogue of Westiellamide

Peter Comba,[a] *Nina Dovalil,*[a,b] *Graeme R. Hanson,*[b,*] *Jeffrey R. Harmer,*[b] *Christopher J. Noble,*[b] *Mark J. Riley,*[c] *Bjoern Seibold*[a]

[a] Universität Heidelberg, Anorganisch-Chemisches Institut, D-69120 Heidelberg, Germany

[b] The University of Queensland, Centre for Advanced Imaging Brisbane, Queensland 4072, Australia

[c] The University of Queensland, School of Chemistry and Molecular Biosciences, Brisbane, Queensland 4072, Australia

Corresponding Author
Prof. Graeme Hanson
Centre for Advanced Imaging
The University of Queensland
Email: Graeme.Hanson@cai.uq.edu.au
Phone: +61-7-3365-3242
Fax: +61-7-3365-3833

Abstract

Three synthetic analogues of westiallamide, H_3L^{wa} have previously been synthesized (H_3L^{1-3}) which have a common backbone (derived from *L*-valine) with H_3L^{wa} but differ in their heterocyclic rings (imidazole, oxazole, thiazole and oxazoline). Herein we explore in detail through high resolution pulsed EPR and MCD spectroscopy in conjunction with density functional theory (DFT) the geometric and electronic structures of the mono- and di-nuclear Cu^{II} complexes of these cyclic pseudo-hexapeptides. Orientation selective HYSCORE, ENDOR and three-pulse ESEEM of $[Cu^{II}(H_2L^1)(MeOH)_2]^+$ reveal delocalization of the unpaired electron spin onto the ligating and distal nitrogens of the coordinated heterocyclic rings and that they are magnetically inequivalent. DFT calculations confirm this and show similar spin densities on the distal heteroatoms in the heterocyclic rings coordinated to the Cu^{II} ion in the other cyclic pseudo-hexapeptide $[Cu^{II}(H_2L^{2,3,wa})(MeOH)_2]^+$ complexes. The magnetic inequivalencies in $[Cu^{II}(H_2L^1)(MeOH)_2]^+$ arise from different orientations of the heterocyclic rings coordinated to the Cu^{II} ion and that delocalization of the unpaired electron onto the distal heteroatoms within these N-methylimidazole rings depend upon their location with respect to the Cu^{II} d_{x2-y2} orbital. A systematic study of DFT functionals and basis sets was undertaken to examine the ability to reproduce the experimentally determined spin Hamiltonian parameters. Inclusion of spin-orbit coupling (SOC) using MAG-ReSpect or ORCA with a BHLYP/IGLO-II Wachters setup with SOC corrections and about 38% Hartree Fock exchange gave the best predictions of the *g* and $A(^{63}Cu)$ matrices. DFT calculations of the ^{14}N hyperfine and quadrupole parameters for the distal nitrogens of the coordinated heterocyclic rings in $[Cu^{II}(H_2L^1)(MeOH)_2]^+$ with the B1LYP functional and the SVP basis set were in excellent agreement with the experimental data, though other choices of functional and basis set also provided reasonable values. MCD, EPR, mass spectrometry and DFT showed that preparation of the dinuclear Cu^{II} complex in a 1:1 MeOH:glycerol mixture (necessary for MCD) resulted in the exchange of the bridging methoxide ligand for glycerol with a corresponding decrease in the magnitude of the exchange coupling.

Introduction

Ascidiacea (ascidians or sea squirts) are sessile filter feeding marine invertebrate animals that are normally found firmly attached to a substratum such as rocks along coastlines or coral reefs, where the water levels are shallow and the salinity is greater than 2.5%.[1-6] They have a sac-like body that incorporates three regions, the pharyngeal, abdomen and postabdomen that is housed within a tough outer "tunic" made of the polysaccharide tunicin, which compared to other tunicates leads to a more rigid “exoskeleton”.[1-6] The pharyngeal region contains the pharynx, which is the basis of the digestive system involving filtering plankton, metal ions and nutrients out of the seawater through its two siphons. The abdomen contains most of the other bodily organs, and the postabdomen contains the heart and gonads.[1-6] Ascidians can be found all over the world, and are among those marine organisms whose Cu^{II} accumulation is high.[7,8] The fact that Cu^{II} is found in non-polar tissue fractions suggests its complexation by low molecular weight organic molecules, such as natural cyclic pseudo-peptides, *e.g.* patellamides or proteins. Indeed, the marine genus *Lissoclinum* is a rich source of cyclic peptide alkaloids, featuring multiple oxazoline, thiazoline, oxazole or thiazole rings that have interesting cytotoxicity, antibacterial and antiviral properties.[8-11] Ascidians live in a symbiotic relationship with prochloron, a unicellular oxygenic photosynthetic prokaryote belonging to the cyanobacteria phylum, and it is thought that they are responsible for the synthesis of these peptides.[12-16] The Cu^{II} coordination chemistry of the native cyclic pseudo octa- and hexa-peptides purified from *L. patella* and *L. bistratum*, respectively and chemically synthesized model cyclic pseudo-peptides for these two classes has been extensively studied.[7,11, 17-28] While the biological function of these cyclic pseudo hexa- and octa-peptides is at present unknown; the fact that there is a diverse range of these peptides and that many[15,16] are synthesized at the ribosome in an archaic symbiont indicates that they have an important biological role. We have previously shown that dinuclear Cu^{II} complexes of cyclic pseudo-octapeptides can catalyze CO_2 fixation (most efficient small molecular weight catalysts known to date) producing carbonate (the backbone of a coral reef),[27] and also mono- and di-phosphoester hydrolysis.[28] Whether or not the corresponding Cu^{II} pseudo-hexapeptide complexes have a metabolic role has to our knowledge not been reported in the literature.

<Insert Chart 1 here>

Westiellamide, a cyclic pseudo-hexapeptide (H_3L^{wa}, Chart 1), that has been isolated from the marine genus *L. bistratum* and from the terrestrial genus *Westiellopsis prolifica*, is known to accumulate in leukemia cells and found to inhibit cytokinesis.[29] In solution, the metal free macrocycle H_3L^{wa} adopts C_3 symmetry (X-ray crystal structures shown in Figure 1), where the

heterocyclic and amide nitrogen atoms point towards the inside of the macrocycle, while the isopropyl residues face to the same side of the macrocycle.[30] The five-membered heterocyclic oxazoline rings result from condensation of threonine side chains with the preceding carbonyl groups of the valine residues in the peptide sequence. Three synthetic analogues (Chart 1) of H_3L^{wa} have been prepared (H_3L^{1-3}) which have a common backbone with H_3L^{wa} but differ solely in their heterocyclic donor groups (N-methylimidazole, oxazole and thiazole, respectively).[31] Plots of their X-ray structures are shown in Figure 1.[30,31] Importantly, the difference in the heterocyclic rings results in subtle differences in the shape of the four macrocycles as the single (sigma) bonds of the oxazoline rings of westiellamide H_3L^{wa} increase the flexibility of the macrocycle.

<Insert Figure 1 here>

Initial studies on the metal complexation of westiellamide were performed by Wipf *et al*., who reported an unusual Ag_4 complex formed with westiellamide.[32] In this complex three of the four Ag^+ ions (coordinated to the oxazoline nitrogens) are located in a pseudo trigonal-planar arrangement about a central Ag^+ ion and all four ions are sandwiched between two westiellamide macrocycles. The central Ag^+ ion is coordinated in a distorted octahedral arrangement by the carbonyl oxygen atoms of the two westiellamide molecules. In addition to the interaction of H_3L^{wa} with Ag^+, Wipf *et al*. also observed weak interactions between westiellamide and other metal ions such as Na^+, Cu^+, Fe^{2+}, Fe^{3+}, Hg^{2+}, Au^{2+} and Zn^{2+}.[32]

Investigations of the interaction of Cu^{II} with H_3L^{wa} and a series of synthetic analogues H_3L^{1-3} (Figure 1) revealed that after addition of base all cyclic pseudo-hexapeptides readily form stable mono- and di-nuclear Cu^{II} complexes.[22] In the absence of base, Cu^{II} forms a 2:1 (H_3L^2:Cu^{II}) complex in which Cu^{II} is coordinated to the outside of the macrocycle through the carbonyl oxygen atoms of the peptide bonds, in a similar manner to the central Ag^+ ion in the unusual [Ag_4-(H_3L^{wa})$_2$] complex reported by Wipf *et al.* [32] Previous investigations of the Cu^{II} coordination chemistry of the cyclic pseudo-hexapeptides H_3L^{1-3}, models for the natural cyclic pseudo-peptide westiellamide H_3L^{wa} revealed interesting differences in their geometric and electronic structures.[22] While all cyclic pseudo-hexapeptides form mononuclear Cu^{II} complexes in the presence of one equivalent of base, Cu^{II} was coordinated to a N_{het}-N_{amide}-N_{het} binding site in H_3L^{1-3} and an N_{het}-N_{amide}-N_{het}-N_{het} binding site in H_3L^{wa} (N_{het}: nitrogen atom of the heterocyclic ring; N_{amide}: deprotonated amide nitrogen). The coordination sphere is completed with one or two axially coordinated solvent molecules. While the binding motif N_{amide}-N_{het}-N_{amide} is also possible, the mononuclear Cu^{II} complexes exhibit a strong

preference for the N_{het}-N_{amide}-N_{het} binding motif, while in the dinuclear Cu^{II} complexes of H_3L^{1-3} the Cu^{II} ions bind to both binding sites and are bridged by either methanol or methoxide which helps stabilize the dinuclear complex.[22] Cu^{II} complexation requires deprotonation of the amide nitrogen(s) and this is metal ion assisted which takes place at relatively low pH values. The protons that are released upon coordination of Cu^{II} acidify the solution, and thus addition of base is mandatory in order to achieve complete complexation.[22,23] Since seawater is slightly basic (pH ~8), it is likely that metal ions are coordinated to these cyclic pseudo-hexapeptides and that these complexes may be involved in metal ion transport or have metabolic roles.

Herein, we have extended our previous continuous wave electron paramagnetic resonance (CW EPR) measurements on the mono- and di-nuclear Cu^{II} complexes of H_3L^{wa} and the series of synthetic analogues $H_3L^{1-3,}$ [22] by undertaking high-resolution pulsed EPR and magnetic circular dichroism (MCD) studies in conjunction with density functional theory (DFT) calculations to further characterize the geometric and electronic structure of the mono- and di-nuclear Cu^{II} complexes of H_3L^{1-3} as structural analogues of westiellamide, H_3L^{wa}. A systematic study of the choice of basis set and functional in DFT calculations was also undertaken to determine their suitability for the calculation of the spin Hamiltonian parameters for the $[Cu^{II}(H_2L^{1-3,wa})(MeOH)_2]^+$ complexes.

Experimental

Materials

Cyclic peptides $H_3L^{1-3,wa}$ were prepared according to published procedures.[10,33] All materials obtained commercially were of reagent grade and used without further purification. Triethylamine was obtained from Wako Chemicals (Tokyo, Japan). Tetrabutylammonium perchlorate and methanol were purchased from Fluka and Aldrich, respectively.

Methods

X-band (ca. 9.5 GHz) CW and pulsed EPR spectra were recorded with a Bruker Biospin Elexsys E580 EPR spectrometer fitted with either a super high Q cavity (CW EPR) or a ER 4118X-MD5 flexline resonator (pulsed EPR). The X-band (~9.4 GHz) CW EPR spectra were recorded under the following conditions: 140 K, modulation frequency 100 kHz, modulation amplitude 0.05 mT, and microwave power 20 mW (10 dB). The magnetic field and microwave frequency were calibrated with a Bruker ER 036TM Teslameter and a Bruker microwave frequency counter, respectively. An Oxford Instruments flow-through cryostat (CF935LT) in conjunction with an Oxford Instruments ITC503 variable-temperature controller provided temperatures of 1.5-50 K at

the sample position in the cavity. Spectrometer tuning, signal averaging, and visualization were accomplished with Bruker's Xepr (version 2.4b.12) software.

Three-pulse electron spin echo envelope modulation (ESEEM) and hyperfine sublevel correlation (HYSCORE)[34,35] experiments were recorded at 5K, 9.67 GHz and employed the pulse sequences $\pi/2$ - τ - $\pi/2$- t_1- $\pi/2$ - τ -echo and $\pi/2$ - τ - $\pi/2$ - t_1 - π - t_2- $\pi/2$ - τ -echo, respectively. The following parameters were used: microwave pulse lengths $t_{\pi/2}$ = 16 ns, t_π = 32 ns, τ = 140 ns, starting times $t_{1,0} = t_{2,0}$ = 400 ns, and time increments of Δt = 40 ns. For three-pulse ESEEM experiments 256 points were collected for each trace and for HYSCORE a 256×256 data matrix was collected. In both three-pulse ESEEM and HYSCORE experiments a four-step phase cycle was used to remove unwanted echoes. All data were processed with MATLAB 2013A (8.1.0.604, The MathWorks, Inc.). The time traces were baseline corrected with an exponential, apodized with a Gaussian window, and zero filled. After a one-dimensional (three-pulse ESEEM) or two-dimensional (HYSCORE) Fourier transformation, absolute-value spectra were calculated. X-band Davies electron nuclear double resonance (ENDOR) spectra were recorded at 9.67 GHz at 5K using the microwave pulse sequence π - T - $\pi/2$ - τ - π - τ - echo with microwave pulses of lengths $t_{\pi/2}$ = 24 ns and t_π = 32 ns, with τ = 400 ns. During time T = 9 μs a radio frequency (RF) pulse of 6 μs was applied using 100% gain of a 150 W Applied Engineering RF amplifier.

CW and pulsed EPR spectra of the mono- and di-nuclear complexes were simulated with the XSophe-Sophe-XeprView[36,37] (version 1.1.4), Molecular Sophe[37,38] (version 2.3.1) and EasySpin[39] computer simulation software suites on a personal computer running the Mandriva Linux v2010.2 operating system. The ENDOR and HYSCORE data were simulated with the program EasySpin[39] using the functions salt and saffron. HYSCORE cross-peak positions (frequencies) were matched to the experimental positions by calculating cross-peak frequencies by diagonalization of a spin Hamiltonian (Eq. 1) with nuclear Zeeman, hyperfine and nuclear quadrupole interactions (no intensity calculation).

High-resolution electrospray ionization mass spectrometry (ESI-MS) was performed with a 9.4 T Bruker ApexQe Qh-ICR hybrid instrument with an Apollo II MTP ion source in the positive-ion electrospray ionization (ESI) mode. Sample solutions in methanol:glycerol (1:1) at concentrations of 10^{-4}–10^{-5}M were admitted to the ESI interface by means of a syringe pump at 5 $mLmin^{-1}$ and sprayed at 4.5 kV with a desolvation gas flow of 2.0 $Lmin^{-1}$ at 25°C and a nebulizer gas flow of 1.0 $Lmin^{-1}$. The ions were accumulated in the storage hexapole for 0.1-1.0 s and then

transferred into the ICR cell. Trapping was achieved at a sidekick potential of -4.0 V and trapping potentials of roughly 1 V. The mass spectra were acquired in the broadband mode with 1M data points. Typically, 16 transients were accumulated for one magnitude spectrum. The instrument was controlled by Bruker ApexControl 2.0.0.beta software and data analysis was performed using the Bruker DataAnalysis 3.4 software.

Density functional theory (DFT) calculations were performed with Gaussian 03,[40] Gaussian 09,[41] TURBOMOLE,[42] ORCA,[43] and MAG-ReSpect.[44] Geometry optimizations were performed using the B3LYP[45,46,47] hybrid functional in combination with the basis sets 6-31g*[47] (C, H N, O, S) and TZVP[48] (Cu). Frequency calculations were performed subsequent to the geometry optimization to confirm the structures were a minimum on the potential energy surface. Using these optimized geometries, we examined a wide range of basis sets and functionals to explore the accuracy in reproducing the experimental spin Hamiltonian matrices for the $[Cu(H_2L^{1,2,3,wa})(MeOH)]^+$ complexes.

Magnetic circular dichroism (MCD) spectra were recorded on an instrument based on a high through-put / high-resolution Jobin Yvon 750s monochromator and an Oxford Instruments SpectroMag superconducting magnet equipped with an SM4 Cryostat using either a Blue (Hamamatsu R7459) PMT (UV) or Si APD (Vis) detector. The MCD spectra were recorded in a methanol:glycerol 1:1 mixture at various temperatures and magnetic fields.

Results and Discussion

EPR Spectroscopy

CW and pulsed EPR experiments are commonly exploited to gain insights into the Cu^{II} ions' geometry, ligating atoms, singly occupied molecular orbital (SOMO) and the extent of delocalization of the unpaired electron spin (i.e. spin density) onto the ligating atoms and atoms within the second coordination sphere.[22,34,49] X-band CW EPR spectra have already been reported and the orthorhombic spin Hamiltonian parameters (g, $A(^{63}Cu)$, $A(^{14}N_{amide})$, $A(^{14}N_{het})$) determined through computer simulation of the first and second derivative EPR spectra are reproduced in Table 1 to allow readers to compare the DFT and EPR results and also the CW EPR and pulsed EPR data presented herein.[22]

< Insert Table 1>

We have extended these CW EPR studies by performing orientation selective pulsed ENDOR and three-pulse ESEEM and HYSCORE experiments[34] to characterize the hyperfine and nuclear quadrupole couplings to the ligating and distal nitrogen's in the N-methylimidazole rings of $[Cu^{II}(H_2L^1)(MeOH)_2]^+$. These techniques provide insights into the extent of delocalization of the unpaired electron onto the heterocyclic rings and peptide backbone. Davies ENDOR spectra (Figure 2c) show signals from strongly coupled ^{14}N nuclei with nuclear (ENDOR) frequencies in the range 15-26 MHz that could be simulated using a model comprising of three nitrogen nuclei, $2 \times N_{het}$ and $1 \times N_{amide}$.[39] These simulations are shown in Figure 2c and the optimized ^{14}N hyperfine and nuclear quadrupole parameters are listed in Table 2. The ^{14}N hyperfine values determined from the ENDOR data are very similar to the values determined previously from the X-band CW EPR data,[22] though in this case the nuclear quadrupole interaction was neglected. Utilizing the g and $A(^{63}Cu)$ matrices determined from the CW EPR spectrum and the $A(^{14}N)$ and $P(^{14}N)$ matrices determined from the ENDOR spectra (Table 2) provides for an accurate simulation of the CW EPR spectrum (Figure 2a,b), though the perpendicular region of the spectrum is very sensitive to the choice of g- and A-strain linewidth parameters.[50-52] The ^{14}N hyperfine and quadrupole parameters (Table 2) for the ligating nitrogen atoms (N_{het} and N_{amide}) are typical of Cu-His (Imidazole) complexes[49,53] and Cu^{II} complexes containing coordinated peptide nitrogens[53,54]. The Davies ENDOR spectrum also reveals ^1H peaks centered around the proton Larmor frequency (Figure 2c, B_0 = 335 mT). The ^1H couplings (~4 MHz) were not included in the simulated spectra and arise from protons within *ca.* 3.4 Å (assuming dipole-dipole coupling). These may be assigned to either the backbone CH or equatorially coordinated MeOH ligands (CH_3 or OH if not deprotonated) moieties. Without additional ^2H exchange data, a unique assignment cannot be made.

< Insert Table 2 and Figure 2 here >

Smaller hyperfine couplings to distal nitrogens in the coordinated imidazole rings of $[Cu^{II}(H_2L^1)(MeOH)_2]^+$ were characterized with orientation selective three-pulse ESEEM and HYSCORE experiments. Surface and contour plots of the HYSCORE spectrum (Figure 3a,b) recorded at the echo maximum of the EPR spectrum (near the g_x / g_y positions) allows the assignment of ^{14}N single-quantum (s) and double-quantum (d) cross-peaks and initial guesses for the hyperfine and nuclear quadrupole couplings. Subscripted atom numbers correspond to those from the DFT calculations (see Figure 5). The experimental HYSCORE (Figure 3a,b) and orientation selective three-pulse ESSEM (Figure 3c – black) spectra clearly show a doubling of the single and double quantum resonances (see N-14a and N-14b, Figure 3b), indicating ^{14}N hyperfine coupling to two different nitrogen nuclei. In addition the HYSCORE spectra (Figure 3a,b) clearly show cross-peaks (label N-34, Figure 3b) from a weakly coupled ^{14}N nucleus. Computer simulation

of the HYSCORE and orientation selective three-pulse ESEEM spectra (Figure 3), assuming the two peaks labeled N-14a and N-14b (Figure 3b) arise from a single nitrogen atom (N-14) in the N-methylimidazole ring (see Figure S4), fails to reproduce the double peaks seen in the experimental spectrum. In contrast, computer simulation of the HYSCORE and orientation selective three-pulse ESEEM spectra with an anisotropic spin Hamiltonian (Eq. 1) with three inequivalent ^{14}N nuclei (N-14a (red), N-14b (purple) and N-34 (green)) and the spin Hamiltonian parameters listed in Table 2 produces simulated spectra (Figures 3b,c) which are in excellent agreement with the experimental spectra. The magnetic inequivalence of the two distal nitrogen nuclei (N-14 and N-34) in the N-methylimidazole rings is also observed in the DFT calculations (see below).[55] The ^{14}N hyperfine interactions have an appreciable isotropic component (A_{iso} (N-14a,b; N-34) = 2.61, 3.00 and 1.10 MHz) signifying that a small percentage of the spin density is delocalized onto the distal nitrogens of the coordinated N-methylimidazole rings of the macrocycle. The origin of the two ^{14}N hyperfine couplings, labeled N-14a and N-14b, will be discussed in conjunction with the DFT studies, below.

< Insert Figure 3 here>

Mims and Peisach produced a plot of P versus the asymmetry parameter (η) and showed that the experimental ^{14}N quadrupole parameters could generally be grouped into three regions, namely A - deprotonated imidazoles; B – imidazoles coordinated to metal ions and C – protonated imidazoles.[56] The ^{14}N quadrupole parameters (Table 2) for the distal nitrogen atoms in the coordinated N-methylimidazole ring in $[Cu^{II}(H_2L^1)(MeOH)_2]^+$ fall just outside of region B, which is clearly not correct and this is attributed to N-methylation of the distal imidazole nitrogen reducing the asymmetry of the electric field gradient at the nitrogen nucleus to almost zero (η=0.09). A similar observation has been observed for Cu^{II} diethylenetriamine substituted imidazole complexes (Im: |P| = 1.43 MHz, η = 0.94; N-MeIm: |P| = 2.06 MHz , η=0.20).[57] This is in contrast to that observed for Cu^{II} centers found in transition metal ion complexes[57] and metalloproteins,[58] for example, phenylalanine hydroxylase[59] and beta amyloid.[60, 61]

A systematic DFT study of square planar Cu^{II} diethylenetriamine imidazole complexes by Ames and Larsen,[55] shows that the magnitude of the distal ^{14}N hyperfine and quadrupole couplings depends on the orientation of the plane of the imidazole ring with respect to the plane of the d_{x2-y2} orbital. Maximal and minimal ^{14}N hyperfine and quadrupole couplings were observed when the ring was perpendicular and parallel to the d_{x2-y2} orbital, respectively.[55] In contrast, the lower symmetry (distorted square pyramidal) of the Cu^{II} center in $[Cu^{II}(H_2L^1)(MeOH)_2]^+$ and the relative position of the distal nitrogens in the coordinated N-methylimidazaole rings (constrained by cyclic peptide)

with respect to Cu^{II} ion yields DFT calculated ^{14}N hyperfine and quadrupole couplings (Tables 2 and 4) which are not in agreement with those of the DFT study of square planar Cu^{II} diethylenetriamine imidazole complexes.[55] Thus the precise nature of the SOMO, orientation of the N-methylimidazole rings and methylation of the distal nitrogens will affect the ^{14}N hyperfine and quadrupole couplings of the ligating and distal nitrogens in the coordinated N-methylimidazole rings.[56]

DFT Calculation of EPR Spin Hamiltonian Parameters

Calculation of spin Hamiltonian parameters using *ab initio* or DFT has become quite routine for many transition metal ion complexes and can lead to many insights into their electronic structure.[62,63] However, a quantitative calculation of the spin Hamiltonian parameters for Cu^{II} complexes is difficult and the resulting values can vary dramatically from the experimentally determined values.[64] To explore the role of the functional and basis set in the calculation of the *g* and *A* matrices for Cu^{II} complexes of H_3L^{1-3} and H_3L^{wa}, we have undertaken a range of DFT calculations utilizing ORCA 2.6[43] and MAG-ReSpect 1.2.[44] These calculations were performed on fully DFT geometry optimized structures (G03,[40] B3LYP/6-31g*) of the respective complexes.

The spin Hamiltonian parameters (*g* and $A(^{63}Cu)$ matrices, Table 1)[22] of the mononuclear Cu^{II} complexes of H_3L^{1-3} and H_3L^{wa} have been determined previously from computer simulation of the CW EPR spectra using the computer simulation software suites XSophe-Sophe-XeprView[36,37] (version 1.1.4) and Molecular Sophe[37,38] (version 2.0.91) in conjunction with the spin Hamiltonian for an isolated paramagnetic center (H_A):

$$H_A = \underline{\boldsymbol{B}} \bullet g \bullet \underline{\boldsymbol{S}}^T + \underline{\boldsymbol{S}} \bullet A(^{63,65}Cu) \bullet \underline{\boldsymbol{I}}^T - g_n \beta_n \underline{\boldsymbol{B}} \bullet \underline{\boldsymbol{I}}^T (^{63,65}Cu) + \sum_{i=1}^{3} (\underline{\boldsymbol{S}} \bullet A(^{14,15}N) \bullet \underline{\boldsymbol{I}}_i^T - g_n \beta_n \underline{\boldsymbol{B}} \bullet \underline{\boldsymbol{I}}_i^T (^{14,15}N)) \quad (1)$$

The computed *g* matrices for $[Cu^{II}(H_2L^1)(MeOH)_2]^+$, derived from DFT calculations with various combinations of functionals and basis sets are listed in Table 3 and shown graphically in Figure 4a. Corresponding Tables and Figures for $[Cu^{II}(H_2L^{2,3,wa})(MeOH)_2]^+$ are given in the Supporting Information (Tables S1-S3 and Figures S1-S3).

< Insert Table 3 here>

The influence of the amount of exact exchange in the functional on the calculated *g* matrices was probed by using pure GGA functionals, functionals with various amounts of exact exchange

(i.e. B3LYP (25% HF) *vs* B1LYP (20% HF)) and modified BXLYP functionals, where X corresponds to the percentage of exact exchange. The functionals: PBE,[65,66] B3PW,[45,67-69] TPSS,[70] B3LYP,[45,46,48] B1LYP,[71] B38LYP, B40LYP and BHLYP in combination with the basis sets SVP,[47] TZV,[48] TZVP,[48] 6-31g*,[72] 6-311g*,[72] IGLO-II,[73] IGLO-III,[73] EPR-II,[74] and Wachters[75] have also been used in the calculations.

There was a large variation in predicted g-values amongst the functionals. The general over-estimation of the *g* shift (especially g_z) has been attributed to a combination of too much covalent bonding and the over prediction of the d-orbital splitting and consequently hybrid functionals like B3LYP (usually with at least 20% Hartree Fock exchange) are certainly to be preferred.[76] However, elevated levels of HF exchange are problematic since they also lead to strong spin contamination.[77]

It was found that increasing the amount of exact exchange to at least 38% is mandatory to obtain g_z values in a reasonable range (Figure 4a). The best agreement of g_z and g_y with the experimentally derived values is obtained using the B40LYP functional. Although in most of the cases the *g* matrices are overestimated by the BHLYP functional (50% HF exchange), this was used for further investigations. BHLYP is a well established functional, and its various dependencies are well understood. Manually changing the amount of HF exchange might have some unforeseen influence on the calculation, and thus the application of an established functional was considered reasonable. The MAG-ReSpect calculated *g* matrices of $[Cu^{II}(H_2L^1)(MeOH)_2]^+$ are in best agreement with the experimentally determined values, especially g_z which is in excellent agreement with the experiment, albeit with a 10 fold increase in computational time.

<Insert Figure 4 here>

The EPR-II basis set of Barone is commonly applied in $A(^{63}Cu)$ matrix calculations.[74] However, for the investigated Cu^{II} complexes of H_3L^{1-3} and H_3L^{wa}, it was found that the basis set limit is reached at the IGLO-II level (Figures 4b, S1-S3 and Tables 3, S1-S3). Utilization of the IGLO-III and EPR-II basis sets basically provided identical results to those of IGLO-II. Analyzing the data (comparison of the experimental and DFT calculated A_i (i=x,y,z) values) it emerges that a basis set without a frozen core region is important as otherwise the A_z values are in good agreement with the experiment but the $A_{x,y}$ values are greatly overestimated (*e.g.* TZVP and 6-31g*). Applying the Wachters basis set to Cu^{II} significantly improves the calculation, reproducing the observed trend

that $A_{x,y}$ is significantly smaller than A_z, yet A_z is overestimated by a factor of about two.[75] This large overestimation is caused by neglecting spin-orbit coupling (SOC) due to Cu^{II} and the results are substantially improved when SOC contributions are included. The calculated $A(^{63}Cu)$ matrices for the Cu^{II} complexes of H_3L^{1-3} and H_3L^{wa} and their dependence on the applied basis sets is shown in Tables 3 and S1-S3 and are depicted in Figures 4b, S1-S3. The inability to accurately define the s-electron spin density at the nucleus (and hence $A_{iso}(^{63}Cu)$) produces inaccurate $A(^{63}Cu)$ matrices (Table 3) and consequently, results in inaccurate $A(^{14}N)$ hyperfine couplings from ligating nitrogen atoms (Table S4). However, Lancaster *et al.* showed that the QM/MM in conjunction with spectroscopy oriented configuration interaction (SORCI) accurately reproduced the g and ^{63}Cu and ^{14}N hyperfine matrices for the type zero Cu^{II} center in variants of *Pseudomonas aeruginosa* azurin.[63] In contrast the $A(^{14}N)$ hyperfine couplings from the distal nitrogen atoms in the N-methylimidazole rings mainly arise from a dipole-dipole interaction. This is confirmed in the calculations of the of the anisotropic $A(^{14}N)$ hyperfine and $P(^{14}N)$ nuclear quadrupole matrices (Table 4), where there is significantly smaller variation and that all of the results are in reasonable agreement with the experimental values (Tables 2 and 4) obtained from the HYSCORE and three-pulse ESEEM spectra. Spin densities (and the ^{14}N hyperfine couplings) on the noncoordinated amide and N-methylimidazole nitrogen atoms are significantly smaller (at least a factor of 10 smaller) than those for distal nitrogen atoms of the coordinated N-methylimidazole ligands (Figure 5). Consequently, a plausible explanation for the observation of two ^{14}N hyperfine couplings, labeled N-14a and N-14b is that there are two confirmations of the coordinated N-methylimidazole ring. Rotation of the ring must be quite small as the difference between the spin Hamiltonian parameters (N-14a vs N-14b) is quite small (Table 2). Confirmation of this would require ^{15}N NMR studies of the paramagnetic Cu^{II} complex, followed by molecular modeling to find the local minima on the potential energy surface and subsequent DFT studies to optimize the geometries and calculate the spin Hamiltonian properties. This is beyond the scope of the current research.

<Insert Table 4 here>

In agreement with the HYSCORE and ESEEM results, the DFT calculations reveal that the distal nitrogens, N-14 and N-34 in the coordinated N-methylimidazole rings are magnetically inequivalent (Table 4), which is reflected in their different spin densities in the singly occupied molecular orbital (SOMO, Figure 5b). The different ^{14}N hyperfine couplings result from the N-methylimidazole ring (containing N-34) being twisted out of the equatorial plane containing the Cu^{II} $d_{x^2-y^2}$ orbital and N-34 being oriented between the Cu-ligand bonds (Figure 5a), rather than approximately along the Cu-ligand bond as for N-14. These factors result in reduced isotropic and anisotropic ^{14}N hyperfine

couplings for N-34. The DFT calculations (Table 4) also reproduce the experimental quadrupole parameters (P, η) indicating that indeed methylation of the distal nitrogen reduces the asymmetry parameter to approximately zero.

<Insert Figure 5 here>

A comparison of the SOMO's for the Cu^{II} complexes ($[Cu^{II}(H_2L^1)(MeOH)_2]^+$, $[Cu^{II}(H_2L^2)(MeOH)_2]^+$, $[Cu^{II}(H_2L^3)(MeOH)_2]^+$ and $[Cu^{II}(H_2L^{wa})(MeOH)_2]^+$) (Figure 5) reveals subtle differences in the amount of spin density on the distal heteroatoms in the rings (N-methylimidazole, oxazole, thiazole and oxazoline) coordinated to the Cu^{II} ion through the nitrogen atom. For all complexes the distal heteroatoms in the two coordinated heterocyclic rings have inequivalent spin densities ($[Cu^{II}(H_2L^1)(MeOH)_2]^+$ - N-14: 3.475 x 10^{-3}, N-34: -5.37 x 10^{-4}; $[Cu^{II}(H_2L^2)(MeOH)_2]^+$ - O-14: 3.631 x 10^{-3}, O-34: 1.98 x 10^{-4}; $[Cu^{II}(H_2L^3)(MeOH)_2]^+$ - S-14: 3.990 x 10^{-3}, S-34: 3.83 x 10^{-4}; $[Cu^{II}(H_2L^{wa})(MeOH)_2]^+$ - O-14: 3.218 x 10^{-3}, O-34: 4.66 x 10^{-4}), which originates from the geometric and electronic factors described above for $[Cu^{II}(H_2L^1)(MeOH)_2]^+$ (Figure 5a,c,e,g). Interestingly, but not unexpected, there is more spin density on the distal sulfur atoms (S-14, S-34) of the coordinated heterocyclic rings as the 3p-orbitals are larger than those for N and O (2p-orbitals) enabling greater delocalization of the unpaired electron spin. While the spin densities are small, the agreement between the experimental and calculated ^{14}N hyperfine and nuclear quadrupole splittings of the distal nitrogen in the heterocyclic rings of $[Cu^{II}(H_2L^1)(MeOH)_2]^+$ is excellent giving confidence in the spin densities for the distal atoms in the heterocyclic rings of the other complexes.

MCD Spectroscopy

An MCD experiment provides simultaneous information about the ground and excited states of a paramagnetic material.[78,79] A spectrum can be observed when circularly polarized light is propagated through a sample positioned within a strong magnetic field parallel to the direction of propagation. The MCD spectrum is detected as the absorbance difference of the substance between left and right circularly polarized light.[80] The general equation that describes the MCD signal is

$$\frac{\Delta\varepsilon}{E} = \frac{\varepsilon_{LCP} - \varepsilon_{RCP}}{E} = \gamma\mu_B B\left[\left(-\frac{\partial f(E)}{\partial E}\right)\overline{A}_1 + \left(\overline{B}_0 + \frac{\overline{C}_0}{kT}\right)f(E)\right] \qquad (2)$$

where γ = is a collection of constants, B = magnetic flux density, k = Boltzman constant, μ_B = Bohr magneton, $f(E)$ = line shape function, T = temperature, ε_{LCP} and ε_{RCP} are the extinction coefficients for left and right circularly polarized light.[78-82] A_1, B_0 and C_0 are characteristic terms that depend on the electronic and geometric structure of the molecule under investigation. Each molecule with

degenerate excited states exhibits an A_1 term with a derivative band shape. While the B_0 term has an absorption like band shape and arises when the applied field causes a mixing of the ground state or an excited state with an intermediate state. The C_0 term is caused by degenerate ground states, and therefore only present in paramagnetic species. It is the only temperature dependent term, dominating the spectra at low temperatures and identifies paramagnetic species.

Variable temperature MCD spectra (Figure 6) of $[Cu^{II}(H_2L^1)(MeOH)_2]^+$ reveal a strong temperature dependence of the signals consistent with a large C_0 term arising from the paramagnetic Cu^{II} center. The MCD saturation curve of the absorption at 700 nm and its fit (red) is shown in the inset to Figure 6. It was fitted assuming $g_z = 2.283$ and an *xy* polarized transition. This is in agreement with the simulated EPR data (Table 1; g_z = 2.278). The MCD spectra of $[Cu^{II}(H_2L^1)(MeOH)_2]^+$ are in good agreement with the experimental findings from the CW and pulsed EPR, UV-vis, and CD spectroscopic studies,[22,83] which are characteristic of a square pyramidal Cu^{II} coordination geometry with Cu^{II} bound to the N_{het}-N_{amide}-N_{het} motif.

<Insert Figure 6 here>

While the EPR measurements and DFT calculations of the geometry and spin state for the dimer $[Cu_2^{II}(L^1)(\mu\text{-OMe})]$ predict a strongly antiferromagnetically coupled species which is EPR silent at 77 K, the MCD data measured in a methanol:glycerol (1:1) glass (Figure 7) are consistent with a weakly coupled species (nested variable temperature variable field curves) and consequently it should be possible to measure an EPR spectrum at 77 K. The possibility that the recorded MCD spectrum arises from an impurity of the monomeric Cu^{II} complex $[Cu^{II}(H_2L^1)(MeOH)_2]^+$ in the sample can be excluded for several reasons. The signal that was recorded for the dimeric complex is strong and the delta absorption values (ΔA) are similar to those of the monomeric species, while a signal arising from an impurity is expected to have considerably smaller delta absorption values. Furthermore, the peak positions and general appearance of the MCD spectra (Figures 6 and 7a) of the mono- and the dinuclear species are significantly different. The mononuclear complex $[Cu^{II}(H_2L^1)(MeOH)_2]^+$ has a negative delta absorption band at 700 nm and a positive delta absorption at 940 nm, whereas the dinuclear Cu^{II} complex of H_3L^1 exhibits two negative delta absorption bands at 550 and 660 nm. Moreover, the variable temperature variable field (VTVH) curves of the dinuclear Cu^{II} complex, measured at 660 nm are nested, which is a strong indication for coupled species (Figure 7b).

<Insert Figure 7 here>

From the experimental variable temperature variable field (VTVH) curves of the dinuclear Cu^{II} complex of H_3L^1, the *g* matrix, exchange coupling constant *J* and the axial (D) and rhombic (E) zero-field splitting values can be derived from a fit of the nested VTVH curves. The VTVH data has been analyzed using the formalism developed by Neese and Solomon, Eq. 3.[78] For a particular coupled spin system S_1 and S_2, the MCD magnetization curves are calculated as:

$$\frac{\Delta A}{E} = -\frac{1}{4\pi S}\int_0^{\pi}\int_0^{2\pi}\sum_i N_i \,(l < S_{xli} > M_{yz1}^{eff} + m < S_{Yli} > M_{xz1}^{eff} + n < S_{zli} > M_{yx1}^{eff} + l < S_{x2i} > M_{yz2}^{eff} + m < S_{y2i} > M_{xz2}^{eff} + n < S_{z2i} > M_{yz2}^{eff}) sin\theta d\theta d\varphi + B_0\, B \qquad (3)$$

where N_i are the Boltzmann populations of the energy levels; $<S_{xli}>$ is the expectation value of the spin operator S_x for spin 1 in level i; and *l*, *m*, *n* specifies the direction of the magnetic field with respect to a fixed molecular axis system, and the integration is carried out numerically over all orientations. The M_{xy}^{eff}, M_{xz}^{eff}, M_{yz}^{eff} are the effective transition dipole moment products for transitions centered on either the S_1 or S_2 metal ion. For a transition allowed in *x* and *y* polarization, one expects $M_{xy}^{eff} \gg M_{xz}^{eff} \sim M_{yz}^{eff}$. The last term describes the field dependent B_0 term of Eq. (2). The population factors N_i and the spin expectation values are calculated from the energies and wavefunctions, respectively, of the spin Hamiltonian for the coupled system

$$H = \sum_{i-1}^{2} H_{Ai} + H_{\text{int}}$$
$$H_{\text{int}} = -2J_{iso}\underline{S}_1 \bullet \underline{S}_2 + \underline{S}_1 \bullet D \bullet \underline{S}_2 \qquad (4)$$

where H_A is given in Eq. 1. The best fit of the experimental data is shown in Figure 7b. For coupled spin systems the D matrix (quantified by zero-field splitting D, E values) is non-zero due to a combination of anisotropic exchange (*J*) and dipole-dipole coupling terms. Without additional structural information about the metal-metal distance and orientation of principal axes, it is difficult to separate these terms. We therefore fitted the dimer VTVH data (Figure 7b) with an effective *S*=1 spin Hamiltonian resulting in the parameters given in Table 5. The quality of the fit indicates that the Cu^{II} ions are not strongly antiferromagnetically coupled as population of the higher S_{Tot}=1 spin state would be observed in the VTVH data. Thus the Cu^{II} ions are either very weakly exchange coupled or strongly ferromagnetically coupled. The only experimental difference between the MCD and EPR silent experiment of the dimer system as described above, was the presence of 50%

glycerol, in order to generate an optically clear glass. Repeating the EPR measurements under these conditions produced the EPR spectrum shown in Figure 8, which arises from the coupled dinuclear Cu^{II} complex. When the temperature is decreased to 10 K, saturation of the EPR transitions is observed, which is consistent with a small exchange coupling (Orbach relaxation[84]), predicted by the MCD measurements.

<Insert Figure 8 here>, <Insert Table 5 here>

The experimental EPR spectrum could be simulated (Figure 8b) with an S=1 spin Hamiltonian (Eq. 4) and the spin Hamiltonian parameters given in Table 5. The corresponding energy level diagrams and transitions along the 'z', 'x' and 'y' principal directions are shown in Figure 8c-e. A mass spectrum of the dinuclear Cu^{II} complex in methanol:glycerol (1:1) reveals peaks (Figure S5a,c) at m/z=825.20358 and 861.05422. Calculated spectra for $[Cu_2^{II}(L^1)(OCH(CH_2OH)_2)MeOH(H_2O)]^+$ (m/z= 861.28658) and $[Cu_2^{II}(HL^1)(OCH(CH_2OH)_2)MeOH]^+$ (m/z=825.26545) (Figures S5b,d) are in excellent agreement, particularly the isotope distributions (Figure S5). Assuming glycerol bridges the two Cu^{II} ions ($[Cu_2^{II}(L^1)(\mu\text{-}OHCH(CH_2OH)_2]^+$) and this leads to reduced exchange coupling, we performed a geometry optimization of the dinuclear complex utilizing DFT methods (B3LYP/6-31g* (C, H, N, O)/TZVP(Cu); Figure 9). This resulted in a calculated exchange coupling constant J_{iso} (-18 cm^{-1}) that was significantly smaller than that for the methoxide bridged dinuclear complex (J_{iso} = -147 cm^{-1}). While the calculation is consistent with the experimental conclusion that the $|J_{iso}|$ value is small, and confirms that glycerol binding modifies the exchange coupling between the Cu^{II} ions and produces different spectroscopic signatures in both the MCD and EPR spectra, there are a number of uncertainties in the orientation of the bridging glycerol and the possibility of additional solvent molecule(s).

<Insert Figure 9 here>

Conclusions

High-resolution EPR spectroscopy in conjunction with density functional theory calculations provides a powerful approach for the geometric and electronic structural characterization of paramagnetic species. Herein we utilized orientation selective pulsed ENDOR, three-pulse ESEEM and HYSCORE in conjunction with DFT calculations and the published CW EPR data to determine the geometric and electronic structure of $[Cu^{II}(H_2L^1)(MeOH)_2]^+$. The electronic structures of the other $[Cu^{II}(H_2L^{2\text{-}3,wa})(MeOH)_2]^+$ complexes were determined by DFT

calculations and utilized the CW EPR data to test the validity of the optimized structure. The geometric structures of $[Cu^{II}(H_2L^{2\text{-}3,wa})(MeOH)_2]^+$ were similar to that of $[Cu^{II}(H_2L^{1})(MeOH)_2]^+$ except the Cu^{II} ions' coordination sphere in $[Cu^{II}(H_2L^{wa})(MeOH)_2]^+$ involved the third oxazoline nitrogen.

Orientation selective ENDOR measurements of $[Cu^{II}(H_2L^{1})(MeOH)_2]^+$ yielded the ligating nitrogen hyperfine and nuclear quadrupole coupling constants (Table 2), which showed that they were magnetically inequivalent, a consequence of the steric constraints of the ligand and the differing nitrogens (amide vs imidazole). The $^{14}N_{het}$ and $^{14}N_{amide}$ quadrupole parameters (Table 2) are in agreement with those in the literature for deprotonated imidazole[58,59] and peptide amide nitrogens.[54,85] These results are consistent with Cu^{II} being coordinated to a N_{het}-N_{amide}-N_{het} binding site in H_3L^1 as suggested from the CW EPR studies.[22]

HYSCORE and orientation selective three-pulse ESEEM measurements on this complex also revealed that the distal nitrogens (N-14 and N-34) in the N-methylimidazole rings coordinated to the Cu^{II} ion were also magnetically inequivalent and that there were two populations (confirmations, N-14a and N-14b) of the N-methylimidazole ring containing N-14. The relatively large magnetic inequivalence between N-14 and N-34 is a consequence of the N-methylimidazole ring (containing N-34) being twisted out of the equatorial plane containing the Cu^{II} $d_{x^2-y^2}$ orbital and being oriented between the Cu-ligand bonds (Figure 5a), rather than approximately along the Cu-ligand as for N-14. These factors result in reduced isotropic and anisotropic ^{14}N hyperfine couplings for N-34, which were confirmed with DFT calculations (Table 4). Similar observations were also observed from the spin densities calculated by DFT for the other complexes ($[Cu^{II}(H_2L^{2})(MeOH)_2]^+$, $[Cu^{II}(H_2L^{3})(MeOH)_2]^+$ and $[Cu^{II}(H_2L^{wa})(MeOH)_2]^+$). While the spin densities on the N_{het}-N_{amide}-N_{het} binding site within $[Cu^{II}(H_2L^{wa})(MeOH)_2]^+$ were similar to the other complexes, there was additional spin density on the third coordinated oxazoline nitrogen. The experimentally determined η parameters (0.09) for the distal nitrogen atoms (Table 2) are consistent with N-methylation of the imidazole rings.

A systematic study of functionals and basis sets that the experimental g, $A(^{63}Cu)$ spin Hamiltonian parameters could be reasonably reproduced with MAG-ReSpect[44] or using ORCA[43] with the BHLYP functional in combination with the basis sets 6-31g* (C, H, N, S, O), TZVP (first coordination sphere), and Wachters (Cu). Importantly, spin-orbit coupling and the incorporation of about 38% Hartree Fock exchange were critical for the accurate prediction of the spin Hamiltonian parameters (g, $A(^{63}Cu)$). Calculation of the distal heterocyclic nitrogen hyperfine and nuclear quadruple couplings were more accurate as the isotropic hyperfine coupling is significantly smaller

and consequently the proportion of Hartree Fock exchange included in the calculation has only a small effect.

At high base concentrations all macrocycles (H_3L^{1-3}) show the formation of dinuclear methanol (methoxide) bridged Cu^{II} complexes.[22] MCD spectroscopy in conjunction with CW EPR and DFT studies have shown that this bridging ligand is labile and that it can be replaced by glycerol. Upon ligand replacement of the bridging ligand with glycerol, there is a dramatic decrease in the antiferromagnetic exchange coupling between the two Cu^{II} centers. Thus, with an appropriate choice of solvent the dinuclear Cu^{II} complexes of H_3L^{1-3} maybe able to hydrolyze CO_2 and phospho mono- and di-esters as has been shown for the corresponding dinuclear Cu^{II} complexes of the cyclic pseudo octapeptides.[27,28] Indeed, preliminary experiments involving the dinuclear Cu^{II} complex with H_3L^1 show that it is capable of hydrolyzing BDNPP (bis(2,4-dinitrophenyl)phosphate). In contrast, the increased flexibility of the oxazoline vs N-methylimidizale, oxazole and thiazole rings enables H_3L^{wa} to form a mononuclear Cu^{II} center in which the three imidazole and one amide nitrogen atoms are ligated to the Cu^{II} center which explains the lack of dinuclear Cu^{II} complexes in the mass spectra.[22] Thus Cu^{II} ion transport, homeostasis and catalysis are possible biological functions for H_3L^{wa} in *L. bistratum* where high Cu^{II} concentrations are present.

Supporting Information

Tables of DFT calculated spin Hamiltonian parameters for $[Cu(H_2L^{2,3,wa})(MeOH)_2]^+$, corresponding plots of spin Hamiltonian parameters vs. functional, HYSCORE and three-pulse ESEEM simulations and mass spectra for the dinuclear Cu^{II} complex. This information is available free of charge via the Internet at http://pubs.acs.org.

Acknowledgements

We would like to thank The University of Queensland and the Ruprecht-Karls-Universität Heidelberg for financial support, Dr. Bodo Martin for critically reading the manuscript and Miss Nina Mehrkens for measuring the mass spectra and performing the preliminary phosphatase hydrolysis experiments. Dr. Jeffrey Harmer thanks the Australian Research Council for an award of a Future Fellowship (FT120100421). We would also like to thank the anonymous referee for encouraging us to reexamine the analysis of the HYSCORE and three-pulse ESEEM data.

References

1. Kott, P., *Mem. Qld. Mus.* **1985,** *23*, 1-440.
2. Kott, P., *Mem. Qld. Mus.* **1990,** *29*, 1-266.
3. Kott, P., *Mem. Qld. Mus.* **1990,** *29*, 267-298.
4. Kott, P., *Mem. Qld. Mus.* **1992,** *32*, 375-620.
5. Kott, P., *Mem. Qld. Mus.* **1992,** *32*, 621-655.
6. Kott, P., *Mem. Qld. Mus.* **2001,** *47*, 1-407.
7. van den Brenk, A. L. *Ph.D. Thesis*; PhD, Thesis, University of Queensland: 1994.
8. Wright, S. H. R., A.; Feldmann, J.; Krupp, E.; Jaspars, M., Marine Metabolites and Metal Ion Chelation. In *Handbook of Marine Products*, Fattorusso, E. G., W.H.; Taglialatela-Scafati, O., Ed. Springer-Verlag: Berlin, 2012; pp 861-892.
9. Davidson, B. S., *Chem. Rev.* **1993,** *93*, 1771-1791.
10. Haberhauer, G.; Rominger, F., *Eur. J. Org. Chem.* **2003**, 3209-3218.
11. Comba, P.; Dovalil, N.; Gahan, L. R.; Hanson, G. R.; Westphal, M., *Dalton Trans.* **2014,** *43*, 1935-1956.
12. Withers, N. V., W.; Lewin, R. A., *Phycologia* **1978,** *17*, 167-171.
13. Kühl, M.; Larkum, A. W. D., In *Cellular Origin and Life in Extreme Habitats* Seckbach, J., Ed. Kluwer Acad. Publ. : Dordrecht, 2002; Vol. 3: Symbiosis, Mechanisms and Model Systems, pp 273-290.
14. Shimada, A. Y., N.; Kanai, S.; Lewin, R.A.; Maruyama, T., *Phycologia* **2003,** *42*, 193-197.
15. Schmidt, E. W.; Nelson, J. T.; Rasko, D. A.; Sudek, S.; Eisen, J. A.; Haygood, M. G.; Ravel, J., *Proc. Natl. Acad. Sci.* **2005,** *102*, 7315-7320.
16. Long, P. F.; Dunlap, W. C.; Battershill, C. N.; Jaspars, M., *ChemBioChem.* **2005,** *6*, 1760-1765.
17. van den Brenk, A. L.; Fairlie, D. P.; Hanson, G. R.; Gahan, L. R.; Hawkins, C. J.; Jones, A., *Inorg. Chem.* **1994,** *33*, 2280-2289.
18. van den Brenk, A. L.; Byriel, K. A.; Fairlie, D. P.; Gahan, L. R.; Hanson, G. R.; Hawkins, C. J.; Jones, A.; Kennard, C. H. L.; Moubaraki, B.; Murray, K. S., *Inorg. Chem.* **1994,** *33*, 3549-3557.
19. Brenk, A. L. v. d.; Tyndall, J. D. A.; Cusack, R. M.; Jones, A.; Fairlie, D. P.; Gahan, L. R.; Hanson, G. R., *J. Inorg. Biochem.* **2004,** *98*, 1857-1866.
20. Comba, P.; Cusack, R.; Fairlie, D. P.; Gahan, L. R.; Hanson, G. R.; Kazmaier, U.; Ramlow, A., *Inorg. Chem.* **1998,** *37*, 6721-6727.
21. Bernhardt, P. V.; Comba, P.; Fairlie, D. P.; Gahan, L. A.; Hanson, G. R.; Lötzbeyer, L., *Chem. Eur. J.* **2002,** *8*, 1527-1536.
22. Comba, P.; Gahan, L. R.; Haberhauer, G.; Hanson, G. A.; Noble, C. J.; Seibold, B.; van den Brenk, A. L., *Chem. Eur. J.* **2008,** *14*, 4393-4403.
23. Comba, P.; Dovalil, N.; Haberhauer, G.; Hanson, G. R.; Karod, Y.; Taura, T., *J. Biol. Inorg. Chem.* **2010,** *15*, 1129-1135.
24. Comba, P.; Dovalil, N.; Hanson, G. R.; Linti, G., *Inorg. Chem.* **2011,** *50*, 5165-5174.
25. Comba, P.; Dovalil, N.; Gahan, L. R.; Haberhauer, G.; Hanson, G. R.; Noble, C. J.; Seibold, B.; Vadivelu, P., *Chem. Eur. J.* **2012,** *18*, 2578-2590.
26. Comba, P.; Dovalil, N.; Haberhauer, G.; Kowski, K.; Mehrkens, N.; Westphal, M., *Z. Allg. Anorg. Chem. (Special Issue Bioinorganic Chemistry)* **2013,** *639*, 1395-1400.
27. Comba, P.; Gahan, L. R.; Hanson, G. R.; Maeder, M.; Westphal, M., *Dalton Trans.* **2014,** *43*, 3144-3152.
28. Comba, P.; Gahan, L. R.; Hanson, G. R.; Westphal, M., *Chem. Comm.* **2012**, 9364-9366.
29. Stanwell, C.; Gescher, A.; Watters, D., *Biochem. Pharm.* **1993,** *45*, 1753-1761.
30. Hambley, T. W.; Hawkins, C. J.; Lavin, M. F.; van den Brenk, A.; Watters, D. J., *Tetrahedron* **1992,** *48*, 341-348.
31. Haberhauer, G.; Drosdow, E.; Oeser, T.; Rominger, F., *Tetrahedron* **2008,** *64*, 1853-1859.

32. Wipf, P.; Venkatraman, S.; Miller, C. P.; Geib, S. J., *Angew. Chem.* **1994,** *106*, 1554-1556.
33. Wipf, P. M., C. P., *J. Am. Chem. Soc.* **1992,** *114*, 10975-10977.
34. Schweiger, A.; Jeschke, G., *Principles of Pulse Electron Paramagnetic Resonance*. Oxford University Press: Oxford, UK, 2001.
35. Hofer, P.; Grupp, A.; Nebenfuhr, H.; Mehring, M., *Chem. Phys. Lett.* **1986,** *132*, 279-282.
36. Hanson, G. R.; Gates, K. E.; Noble, C. J.; Griffin, M.; Mitchell, A.; Benson, S., *J. Inorg. Biochem.* **2004,** *98*, 903-316.
37. Hanson, G. R.; Noble, C. J.; Benson, S., XSophe - Sophe - XeprView and Molecular Sophe Computer simulation software suites for the analysis of continuous wave and pulsed EPR and ENDOR spectra. In *EPR of Free Radicals in Solids: Trends in Methods and Applications*, Lund, A.; Shiotani, M., Eds. Springer: Heidelberg, 2013; p 223.
38. Hanson, G. R.; Noble, C. J.; Benson, S., Molecular Sophe, An Integrated Approach to the Structural Characterization of Metalloproteins - The Next Generation of Computer Simulation Software. In *High Resolution EPR: Applications to Metalloenzymes and Metals in Medicine"*, Hanson, G. R.; Berliner, L. J., Eds. 2009; Vol. 28, pp 105-174.
39. Stoll, S.; Schweiger, A., *J. Magn. Res.* **2006,** *178*, 42-55.
40. Frisch, M. J.; Trucks, G. W.; Schlegel, H. B.; Scuseria, G. E.; Robb, M. A.; Cheeseman, J. R.; Montgomery Jr., J. A.; Vreven, T.; Kudin, K. N.; Burant, J. C.; Millam, J. M.; Iyengar, S. S.; Tomasi, J.; Barone, V.; Mennucci, B.; Cossi, M.; Scalmani, G.; Rega, N.; Petersson, G. A.; Nakatsuji, H.; Hada, M.; Ehara, M.; Toyota, K.; Fukuda, R.; Hasegawa, J.; Ishida, M.; Nakajima, T.; Honda, Y.; Kitao, O.; Nakai, H.; Klene, M.; Li, X.; Knox, J. E.; Hratchian, H. P.; Cross, J. B.; Bakken, V.; Adamo, C.; Jaramillo, J.; Gomperts, R.; Stratmann, R. E.; Yazyev, O.; Austin, A.; Cammi, R.; Pomelli, C.; Ochterski, J. W.; Ayala, P. Y.; Morokuma, K.; Voth, G. A.; Salvador, P.; Dannenberg, J. J.; Zakrzewski, V. G.; Dapprich, S.; Daniels, A. D.; Strain, M. C.; Farkas, O.; Malick, D. K.; Rabuck, A. D.; Raghavachari, K.; Foresman, J. B.; Ortiz, J. V.; Cui, Q.; Baboul, A. G.; Clifford, S.; Cioslowski, J.; Stefanov, B. B.; Liu, G.; Liashenko, A.; Piskorz, P.; Komaromi, I.; Martin, R. L.; Fox, D. J.; Keith, T.; Al-Laham, M. A.; Peng, C. Y.; Nanayakkara, A.; Challacombe, M.; Gill, P. M. W.; Johnson, B.; Chen, W.; Wong, M. W.; Gonzalez, C.; Pople, J. A. *Gaussian 03, Revision B.03*, Gaussian Inc.: Wallingford CT, 2003.
41. Frisch, M. J.; Trucks, G. W.; Schlegel, H. B.; Scuseria, G. E.; Robb, M. A.; Cheeseman, J. R.; Scalmani, G.; Barone, V.; Mennucci, B.; Petersson, G. A.; Nakatsuji, H.; Caricato, M.; Li, X.; Hratchian, H. P.; Izmaylov, A. F.; Bloino, J.; Zheng, G.; Sonnenberg, J. L.; Hada, M.; Ehara, M.; Toyota, K.; Fukuda, R.; Hasegawa, J.; Ishida, M.; Nakajima, T.; Honda, Y.; Kitao, O.; Nakai, H.; Vreven, T.; Montgomery Jr., J. A.; Peralta, J. E.; Ogliaro, F.; Bearpark, M.; Heyd, J. J.; Brothers, E.; Kudin, K. N.; Staroverov, V. N.; Kobayashi, R.; Normand, J.; Raghavachari, K.; Rendell, A.; Burant, J. C.; Iyengar, S.; Tomasi, J.; Cossi, M.; Rega, N.; Millam, N. J.; Klene, M.; Knox, J. E.; Cross, J. B.; Bakken, V.; Adamo, C.; Jaramillo, J.; Gomperts, R.; Stratmann, R. E.; Yazyev, O.; Austin, A. J.; Cammi, R.; Pomelli, C.; Ochterski, J. W.; Martin, R. L.; Morokuma, K.; Zakrzewski, V. G.; Voth, G. A.; Salvador, P.; Dannenberg, J. J.; Dapprich, S.; Daniels, A. D.; Farkas, O.; Foresman, J. B.; Ortiz, J. V.; Cioslowski, J.; Fox, D. J. *Gaussian 09, Revision A.02*, Gaussian, Inc.: Wallingford CT, 2009.
42. Furche, F.; Ahlrichs, R.; Hättig, C.; Klopper, W.; Sierka, M.; Weigend, F., *WIREs Comput. Mol. Sci.* **2014,** *4*, 91-100.
43. Neese, F., *Comput. Mol. Sci.* **2012,** *2*, 73-78.
44. Malkin, V. G.; Malkina, O. L.; Reviakine, R.; Arbuznikov, A. V.; Kaupp, M.; Schimmelpfennig, B.; Malkin, I.; Helgaker, T.; Ruud, K. *MAG-ReSpect 1.2*.
45. Becke, A. D., *Phys. Rev. A.* **1988,** *38*, 3098-3100.
46. Lee, C.; Yang, W.; Parr, R. G., *Phys. Rev. B* **1988,** *37*, 785-789.
47. Schäfer, A.; Horn, H.; Ahlrichs, R., *J. Chem. Phys.* **1992,** *97*, 2571-2577.
48. Schäfer, A.; Huber, C.; Ahlrichs, R., *J. Chem. Phys.* **1994,** *100*, 5829-5835.

49. Antholine, W. E.; Bennett, B.; Hanson, G. R., Copper Coordination Environments. In *Multifrequency Electron Paramagnetic Resonance*, Misra, S. K., Ed. Wiley-VCH: Verlag, GmbH, 2011; pp 647-718.
50. Froncisz, W.; Hyde, J. S., *The Journal of chemical physics* **1980,** *73*, 3123-3131.
51. Hyde, J. S.; Froncisz, W., *Annual review of biophysics and bioengineering* **1982,** *11*, 391-417.
52. Pilbrow, J. R., *Journal of magnetic resonance (1969)* **1984,** *58*, 186-203.
53. Pogni, R.; Dellalunga, G.; Basosi, R., *Journal of the American Chemical Society* **1993,** *115*, 1546-1550.
54. Edmonds, D. T., *Physics Reports* **1977,** *29*, 233-290.
55. Ames, W. M.; Larsen, S., C., *Phs. Chem. Chem. Phys.* **2009,** *11*, 8266-8274.
56. Mims, W. B.; Peisach, J., ESEEM and LEFE of Metalloproteins and Model Complexes. In *Advanced EPR Applications in Biology and Biochemistry*, Hoff, A. J., Ed. Elsevier: Amsterdam, 1989; pp 1-57.
57. Jiang, F.; McCracken, J.; Peisach, J., *Journal of the American Chemical Society* **1990,** *112*, 9035-9044.
58. Deligiannakis, Y.; Louloudi, M.; Hadjiliadis, N., *Coordination chemistry reviews* **2000,** *204*, 1-112.
59. McCracken, J.; Pember, S.; Benkovic, S. J.; Villafranca, J. J.; Miller, R. J., *Journal of the American Chemical Society* **1988,** *110*, 1069-1074.
60. Drew, S. C.; Noble, C. J.; Masters, C. L.; Hanson, G. R.; Barnham, K. J., *Journal of the American Chemical Society* **2009,** *131*, 1195-1207.
61. Drew, S. C.; Barnham, K. J., *Accounts of chemical research* **2011,** *44*, 1146-1155.
62. De Visser, S. P.; Quesne, M. G.; Martin, B.; Comba, P.; Ryde, U., *Chem. Comm.* **2014,** *50*, 262-282.
63. Lancaster, K. M.; Zaballa, M.-E.; Sproules, S.; Sundararajan, M.; DeBeer, S.; Richards, J. H.; Vila, A. J.; Neese, F.; Gray, H. B., *Journal of the American Chemical Society* **2012,** *134*, 8241-8253.
64. Atanasov, M.; Comba, P.; Martin, B.; Müller, V.; Rajaraman, G.; Rohwer, H.; Wunderlich, S., *J. Comp. Chem.* **2006,** *27*, 1263-1277.
65. Perdew, J. P.; Burke, K.; Ernzerhof, M., *Phys. Rev. Lett.* **1996,** *77*, 3865-3868.
66. Perdew, J. P.; Burke, K.; Ernzerhof, M., *Phys. Rev. Lett.* **1998,** *80*, 891.
67. Perdew, J. P.; Chevary, J. A.; Vosko, S. H.; Jackson, K. A.; Pederson, M. R.; Singh, D. J.; Fiolhais, C., *Phys. Rev. B* **1992,** *46*, 6671-6687.
68. Perdew, J. P.; Chevary, J. A.; Vosko, S. H.; Jackson, K. A.; Pederson, M. R.; Singh, D. J.; Fiolhais, C., *Phys. Rev. B* **1993,** *48*, 4978.
69. Perdew, J. P.; Burke, K.; Wang, Y., *Phys. Rev. B* **1996,** *54*, 16533-16539.
70. Tao, J. M.; Perdew, J. P.; Staroverov, V. N.; Scuseria, G. E., *Phs. Rev. Lett.* **2003,** *91*, 146401-1-146401-4.
71. Adamo, C.; Barone, V., *Chem. Phys. Lett.* **1997,** *274*, 242-250.
72. Hehre, W. J.; Ditchfield, R.; Pople, J. A., *J. Chem. Phys.* **1972,** *56*, 2257-2261.
73. Kutzelnigg, W.; Fleischer, U.; Schindler, M., The IGLO-Method: Ab-initio Calculation and Interpretation of NMR Chemical Shifts and Magnetic Susceptibilities. In *NMR Basic Principles and Progress* Diehl, P., Fluck, E., Kosfeld, R, Ed. Springer-Veralg: Berlin, Germany, 1991; Vol. 23, pp 165-262.
74. Barone, V., Structure, Magnetic Properties and Reactivities of Open-Shell Species From Density Functional and Self-Consistent Hybrid Methods. In *Recent Advances in Density Functional Methods (Part I)* Chong, D. P., Ed. World Scientific: Singapore, 1996; Vol. 1, pp 287-334.
75. Watchers, A. J. H., *J. Chem. Phys.* **1970,** *52*, 1033-1036.
76. Neese, F., *J. Chem. Phys.* **2001,** *115*, 11080-11096.
77. Kaupp, M.; Reviakine, R.; Malkina, O. L.; Arbuznikov, A.; Schimmelpfennig, B.; Malkin, V. G., *J. Comput. Chem.* **2002,** *23*, 794-803.

78. Neese, F.; Solomon, E. I., *Inorg. Chem.* **1999,** *38*, 1847-1865.
79. Osborne, G. A.; Stephens, P. J., *J. Chem. Phys.* **1972,** *56*, 609-618.
80. Piepho, S. B.; Schatz, P. N., *Group Theory in Spectroscopy with Applications to Magnetic Circular Dichroism*. John Wiley and Sons: New York, USA, 1983.
81. Stephens, P. J., *J. Chem. Phys.* **1970,** *52*, 3489-3516.
82. Stephens, P. J., *Chem. Phys. Lett.* **1968,** *2*, 241-244.
83. Seibold, B. Kupfer(II)-Koordinationschemie zyklischer [24]Azakrone-8- und [18]Azakrone-6-Peptide Ruprecht Karls Universitat, 2008.
84. Pilbrow, J. R., *Transition Ion Electron Paramagnetic Resonance*. Clarendon Press: Oxford, 1990.
85. Grimaldi, S.; MacMillan, F.; Ostermann, T.; Ludwig, B.; Michel, H., *Biochemistry (Easton)* **2001,** *40*, 1037-1043.

Tables

Table 1 Anisotropic spin Hamiltonian parameters for the mononuclear complexes $[Cu^{II}(H_2L^1)(MeOH)_2]^+$, $[Cu^{II}(H_2L^2)(MeOH)_2]^+$, $[Cu^{II}(H_2L^3)(MeOH)_2]^+$ and $[Cu^{II}(H_2L^{wa})(MeOH)_2]^+$.[22, a]

	$[Cu^{II}(H_2L^1)]^+$	$[Cu^{II}(H_2L^2)]^+$	$[Cu^{II}(H_2L^3)]^+$	$[Cu^{II}(H_2L^{wa})]^+$
g_x	2.088	2.083	2.082	2.083
g_y	2.051	2.034	2.037	2.051
g_z	2.278	2.279	2.263	2.267
$\|A_x\|$ (^{63}Cu)	17.0	17.3	15.7	14.0
$\|A_y\|$ (^{63}Cu)	15.4	17.2	19.9	16.2
$\|A_z\|$ (^{63}Cu)	153.4	153.0	150.0	175
$\|A_x\|$ ($^{14}N_{het}$)	14.5	15.7	14.3	12.4
$\|A_y\|$ ($^{14}N_{het}$)	7.1	7.1	7.0	6.2
$\|A_z\|$ ($^{14}N_{het}$)	9.0	9.0	9.0	10.4
$\|A_x\|$ ($^{14}N_{amide}$) (+ $^{14}N_{het}$) [b]	13.2	13.4	11.5	16.5
$\|A_y\|$ ($^{14}N_{amide}$) (+ $^{14}N_{het}$) [b]	15.2	14.1	15.7	12.7
$\|A_z\|$ ($^{14}N_{amide}$) (+ $^{14}N_{het}$) [b]	9.5	9.5	9.5	13.4

[a] The ^{63}Cu and ^{14}N hyperfine values (10^{-4} cm^{-1}) were determined from computer simulation of the CW EPR spectra assuming two magnetically equivalent nitrogen ($^{14}N_{het}$) nuclei. The nuclear quadrupole interaction was ignored; [b] for $[Cu^{II}(H_2L^{wa})]^+$.

Table 2. Anisotropic spin Hamiltonian parameters for $[Cu^{II}(H_2L^1)(MeOH)_2]^+$ determined from computer simulation of the orientation selective ENDOR, three-pulse ESEEM and HYSCORE spectra.[a]

Nucleus / Parameter	N_{het}	N_{het}	N_{amide}	N_{distal}-14a	N_{distal}-14b	N_{distal}-34
$\lvert A_x \rvert$ (^{14}N)	38.0	39.0	44.0	2.5	2.9	1.0
$\lvert A_y \rvert$ (^{14}N)	37.0	37.5	35.0	2.5	2.9	1.0
$\lvert A_z \rvert$ (^{14}N)	37.5	38.5	38.5	2.8	3.2	1.3
$\alpha^{o\,b}$	0	0	0	0	0	0
$\beta^{o\,b}$	0	0	0	0	0	0
$\gamma^{o\,b}$	25	245	135	65	65	205
P (^{14}N)^{c}	-3.2	-3.2	3.0	-2.54	-2.40	-2.40
η (^{14}N)^{c}	-0.63	-0.63	-0.67	0.09	0.09	0.09
$\alpha^{o\,b}$	0	0	0	0	0	0
$\beta^{o\,b}$	20	20	0	20	20	20
$\gamma^{o\,b}$	25	245	135	65	65	205

[a)] Units for A (^{14}N) and P (^{14}N) values are MHz which can be converted to 10^{-4} cm^{-1} by dividing the value by 2.99792; [b)] Euler angles (α, β, γ) correspond to a rotation about the '*gz'* axis, a rotation about the new '*gx'* axis and a rotation about the new '*gz'* axis, respectively; [c)] Principal values of the nuclear quadupole tensor **P** are: $e^2qQ/h(4I(2I-1))[-(1-\eta), -(1+\eta), 2]$, $I = 1$, $P = e^2qQ/h$ and η varies between 0 and 1.

Table 3. Calculated and experimental *g* and $A(^{63}Cu)$ values for the mononuclear Cu^{II} complex $[Cu^{II}(H_2L^1)(MeOH)_2]^+$. Calculated with program packages MAG-ReSpect[44] and ORCA.[43] The dependence of the *g* factors on the functional is reflected in the large deviation of the calculated values. The most accurate (sum of differences between experiment and calculated) predicted parameters are denoted in bold.

	g values			$A(^{63}Cu)$ - values[a]		
	g_x	g_y	g_z	$\|A_x\|$	$\|A_y\|$	$\|A_z\|$
Experimental values[22]	2.088	2.051	2.278	15	17	153
Functional / Basis set						
PBE / SVP	2.027	2.039	2.105	49	63	131
PBE / 6-311g*	2.026	2.036	2.101	61	73	122
TPSS / 6-311g*	2.026	2.035	2.097	61	76	129
TPSS / 6-311g* [b] TZVP [c,d]	2.029	2.040	2.104	93	110	111
B3PW / 6-311g*	2.041	2.052	2.148	63	79	161
B3PW / 6-311g* [b] TZVP [c,d]	2.046	2.059	2.163	94	111	146
B3LYP / 6-311g* [b] Wachters [d]	2.043	2.055	2.155	3	19	252
B3LYP / 6-311g*	2.040	2.051	2.146	65	81	153
B1LYP / SVP	2.046	2.059	2.163	47	66	182
B1LYP / SVP [b] Wachters [d]	2.047	2.061	2.171	67	84	168
B38LYP / IGLO-II [b] Wachters [d]	2.071	2.084	2.248	10	30	290
B40LYP / IGLO-II [b] Wachters [d]	2.074	2.088	2.259	9	30	295
B40LYP / IGLO-III [b] Wachters [d]	2.072	2.085	2.254	11	29	294
BHLYP / IGLO-II [b] Wachters [d]	2.085	2.100	2.304	10	33	312
BHLYP / EPR-II [b] Wachters [d]	2.084	2.099	2.303	10	34	312
BHLYP / IGLO-II [b] TZVP [c] Wachters [d]	2.090	2.100	2.310	10	33	312
BHLYP / IGLO-II [b] Wachters [d] SOC	**2.100**	**2.080**	**2.306**	**13**	**31**	**175**
MAG-ReSpect (BHandHLYP / TZVP)	**2.093**	**2.076**	**2.278**	**21**	**5**	**133**

(a) Units, 10^{-4} cm^{-1}; (b) C, H, N, O; (c) first coordination sphere; (d) Cu.

Table 4. Experimental and calculated (ORCA[43]) $A(^{14}N)$ and $P(^{14}N)$ values for the mononuclear Cu^{II} complex $[Cu^{II}(H_2L^1)(MeOH)_2]^+$.[a] The most accurate (sum of differences between experiment and calculated) predicted parameters are denoted in bold.

Atom Number[b] / Functional/Basis sets	N_{distal}-14					N_{distal}-34				
	$\|A_x\|$	$\|A_y\|$	$\|A_z\|$	P	η	$\|A_x\|$	$\|A_y\|$	$\|A_z\|$	P	η
Experimental Values[c]	2.5 2.9	2.5 2.9	2.8 3.2	-2.54 -2.40	0.09 0.09	1.0	1.0	1.3	-2.4	0.09
BHLYP IGLO-II Cu wachters	1.5044	1.6332	2.1378	-2.753	0.122	0.3185	0.4379	0.7509	-2.73	0.089
B1LYP 6311gs	1.6419	1.7922	2.451	-2.498	0.128	0.2494	0.4052	0.7379	-2.466	0.095
B1LYP 6311gs Cu wachters	1.5919	1.7403	2.3802	-2.498	0.128	0.2301	0.3883	0.7185	-2.465	0.095
PBE 6311g*	1.6945	1.89	2.6426	-2.517	0.142	0.3005	0.4736	0.7802	-2.467	0.129
PBE 6311g* TZV	1.7284	1.9272	2.6298	-2.527	0.144	0.3802	0.554	0.8657	-2.477	0.132
TPSS 6311g*	1.6222	1.8085	2.5868	-2.503	0.136	0.1918	0.3716	0.6912	-2.456	0.133
TPSS 6311g* TZV	1.6506	1.8387	2.5653	-2.513	0.139	0.2687	0.4471	0.7698	-2.465	0.118
B3PW 6311g*	1.727	1.8839	2.5745	-2.517	0.133	0.2351	0.4091	0.7405	-2.485	0.107
B3PW 6311g* TZV	1.7093	1.8687	2.516	-2.526	0.137	0.2615	0.4402	0.7732	-2.493	0.112
B3LYP 6311g*	1.6915	1.85	2.5417	-2.494	0.13	0.2599	0.421	0.7549	-2.458	0.1
B1LYP SVP	**2.451**	**2.6075**	**3.2561**	**-2.542**	**0.126**	**0.3016**	**0.4958**	**0.8233**	**-2.511**	**0.097**
B1LYP 6311g+ wachters	1.5919	1.7403	2.3802	-2.498	0.128	0.2301	0.3883	0.7185	-2.465	0.095
BHLYP EPRII Cu wachters	1.5039	1.6262	2.1294	-2.678	0.119	0.2752	0.4032	0.7169	-2.665	0.083

[a] Anisotropic ^{14}N hyperfine (A) and quadrupole (P) parameters have units of MHz. [b] Nitrogen atom numbers are given in red in Figure 5. [c] There are two sets of parameters for N_{distal}-14, potentially arising from two different confirmations of the imidazole ring.

Table 5. Experimentally determined parameters from MCD and EPR for the coupled dimer $[Cu_2^{II}(L^1)(\mu\text{-}OHCH(CH_2OH)_2)]^+$ complex in a methanol:glycerol (1:1) solvent mixture, treating it as an effective S=1 spin system (see text).[a] The parameters simultaneously fit the MCD (Figure 7b) and the EPR (Figure 8b) except for $|A_i|$ (^{63}Cu) (EPR only) and B_0 (MCD only).

Parameter	Value
g_x [a]	2.121
g_y [a]	2.155
g_z [a]	2.130
$\|A_x\|$ (^{63}Cu) [a]	20.3×10^{-4} cm^{-1}
$\|A_y\|$ (^{63}Cu) [a]	21.6×10^{-4} cm^{-1}
$\|A_z\|$ (^{63}Cu) [a]	150×10^{-4} cm^{-1}
D	0.0185 cm^{-1}
E/|D|	0.220
B_0	-0.0011 T^{-1}

[a] The g- and A-values refer to an effective S=1 spin Hamtionian (Eq. 4) of a Cu^{II} dimer system.

Figures

Figure 1. X-ray structures[30, 31] of H_3L^1, H_3L^2, H_3L^3 and H_3L^{wa} showing the top (top) and side (bottom) views. Atom colours: nitrogen - blue, oxygen - red, carbon - grey, sulfur – yellow. Hydrogen atoms and solvent molecules have been omitted for clarity. Blue, red and green heterocyclic rings correspond to N-methylimidazole, oxazole/oxazoline and thiazole rings, respectively.

Figure 2. CW EPR and Davies ENDOR spectra of $[Cu^{II}(H_2L^1)(MeOH)_2]^+$ in methanol. (a) Second derivative X-band CW EPR spectrum (red) and (b) the corresponding simulation (blue). (c) X-band (ν = 9.672 GHz) Davies ENDOR spectra (black) recorded at 5.0 K at the indicated field positions along with the simulations (total blue) for three strongly coupled ^{14}N nuclei (green, red and magenta). Spin Hamiltonian parameters are given in Table 2. The vertical lines show the ^1H Lamor frequency and these proton resonances, were not simulated.

Figure 3. X-band (ν = 9.671 GHz) HYSCORE (335.0 mT) and orientation selective 3-pulse ESEEM spectra of $[Cu^{II}(H_2L^1)(MeOH)_2]^+$ in methanol recorded at 5.0K. (a,b) Surface and contour plots showing the HYSCORE spectrum. (b) A contour plot showing an overlay of the experimental and simulated HYSCORE spectra. ^{14}N single- and double-quantum cross-peaks are labeled 's' and 'd', respectively. A selection of simulated cross-peaks are labeled for three distal ^{14}N atoms (N-14a (red), N-14b (purple) and N-34 (green)). Atom numbers correspond to those given in Figure 5. For reference the nitrogen Larmor frequency is $\nu(^{14}N)$ = 1.03 MHz. (c) Orientation selective three-pulse ESEEM spectra (black) recorded at the indicated field positions along with the simulations (blue) for the distal nitrogens. Spin Hamiltonian parameters determined from the simulation of both the HYSCORE and three-pulse ESEEM spectra are given in Table 2.

Figure 4. Calculated and experimental (a) g and (b) $|A|$ (^{63}Cu) matrices for $[Cu^{II}(H_2L^1)(MeOH)_2]^+$ calculated with various combinations of functionals and basis sets with the programs ORCA[43] and MAG-ReSpect.[44] The experimental values are depicted as horizontal lines.

Figure 5. Structures and SOMO's for (a,b) $[Cu^{II}\ H_2L^1)(MeOH)_2]^+$, (c,d) $[Cu^{II}(H_2L^2)(MeOH)_2]^+$, (e,f) $[Cu^{II}(H_2L^3)(MeOH)_2]^+$ and (g,h) $[Cu^{II}(H_2L^{wa})(MeOH)_2]^+$ showing delocalization of the unpaired electron onto the N-methylimidazole, thiazole, oxazole and oxazoline rings of the [18]azacrown-6 macrocyclic rings. Nitrogen atom numbers given in red.

Figure 6. Variable temperature MCD spectra of $[Cu^{II}(H_2L^1)(MeOH)_2]^+$ measured at 5 T in methanol:glycerol (1:1) frozen solution, $c(H_3L^1) = 30$ mM. Inset: VTVH saturation curves at $\lambda = 700$ nm, experimental (black crosses) and simulated (red lines). All curves are overlaying.

Figure 7. Variable temperature MCD spectra of $[Cu_2^{II}(L^1)(\mu\text{-}OHCH(CH_2OH)_2)]^+$. (a) Experimental spectra measured at 5T in methanol:glycerol (1:1) frozen solution, ($c(H_3L^1) = 30$ mM), (b) Variable temperature variable field curves (black = experimental, red = fit; $\lambda = 660$ nm; T = 1.75 K – 50 K, measured at 7 T. Spin Hamiltonian parameters are given in Table 5.

Figure 8 X-Band EPR spectra of $[Cu_2^{II}(L^1)(\mu\text{-}OHCH(CH_2OH)_2)]^+$. (a) Experimental EPR spectrum of $[Cu_2^{II}(L^1)(\mu\text{-}OHCH(CH_2OH)_2)]^+$ in a methanol:glycerol (1:1) frozen solution, $c(H_3L^1) = 1.5$ mM, $\nu = 9.434401$ GHz, T = 50 K, (b) computer simulation of (a). (c-e) Energy level diagrams showing the allowed EPR transitions along the 'z', 'x' and 'y' principal directions, respectively. Spin Hamiltonian parameters are given in Table 5.

Figure 9. DFT calculated structure (Gaussian03,[40] B3LYP/6-31g*/TZVP) of the glycerol bridged dinuclear Cu^{II} complex $[Cu_2^{II}(L^1)(\mu\text{-}OHCH(CH_2OH)_2]^+$.

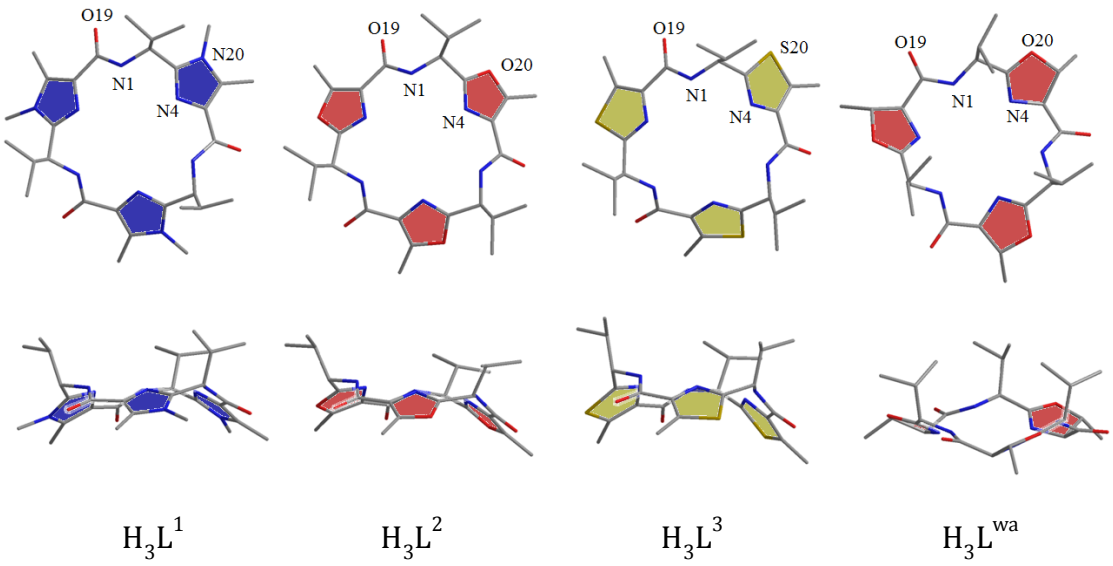

Figure 1. X-ray structures[30, 31] of H_3L^1, H_3L^2, H_3L^3 and H_3L^{wa} showing the top (top) and side (bottom) views. Atom colours: nitrogen - blue, oxygen - red, carbon - grey, sulfur – yellow. Hydrogen atoms and solvent molecules have been omitted for clarity. Blue, red and green heterocyclic rings correspond to N-methylimidazole, oxazole/oxazoline and thiazole rings, respectively.

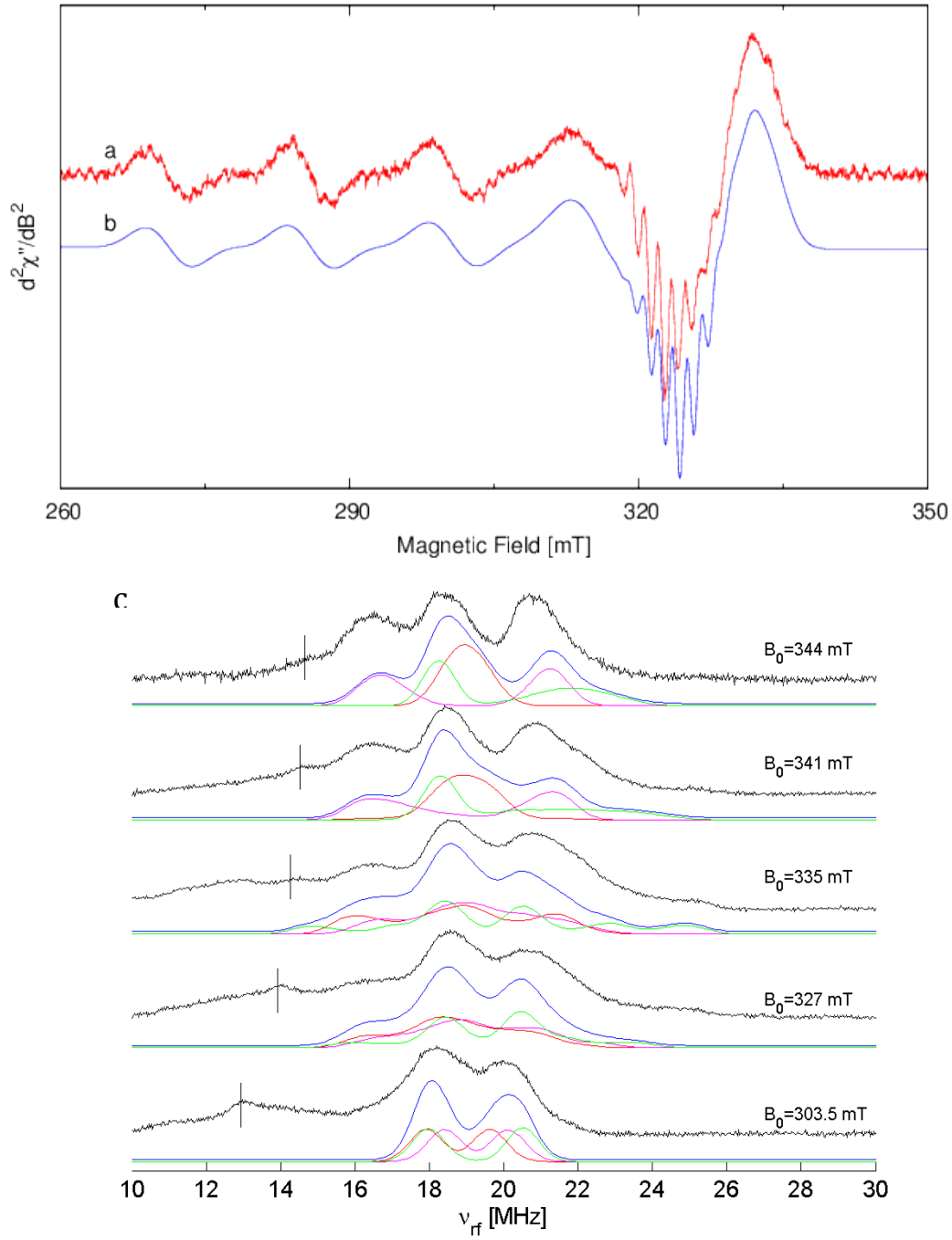

Figure 2. CW EPR and Davies ENDOR spectra of $[Cu^{II}(H_2L^1)(MeOH)_2]^+$ in methanol. (a) Second derivative X-band CW EPR spectrum (red) and (b) the corresponding simulation (blue). (c) X-band (ν = 9.672 GHz) Davies ENDOR spectra (black) recorded at 5.0 K at the indicated field positions along with the simulations (total blue) for three strongly coupled ^{14}N nuclei (green, red and magenta). Spin Hamiltonian parameters are given in Table 2. The vertical lines show the ^1H Lamor frequency and these proton resonances, were not simulated.

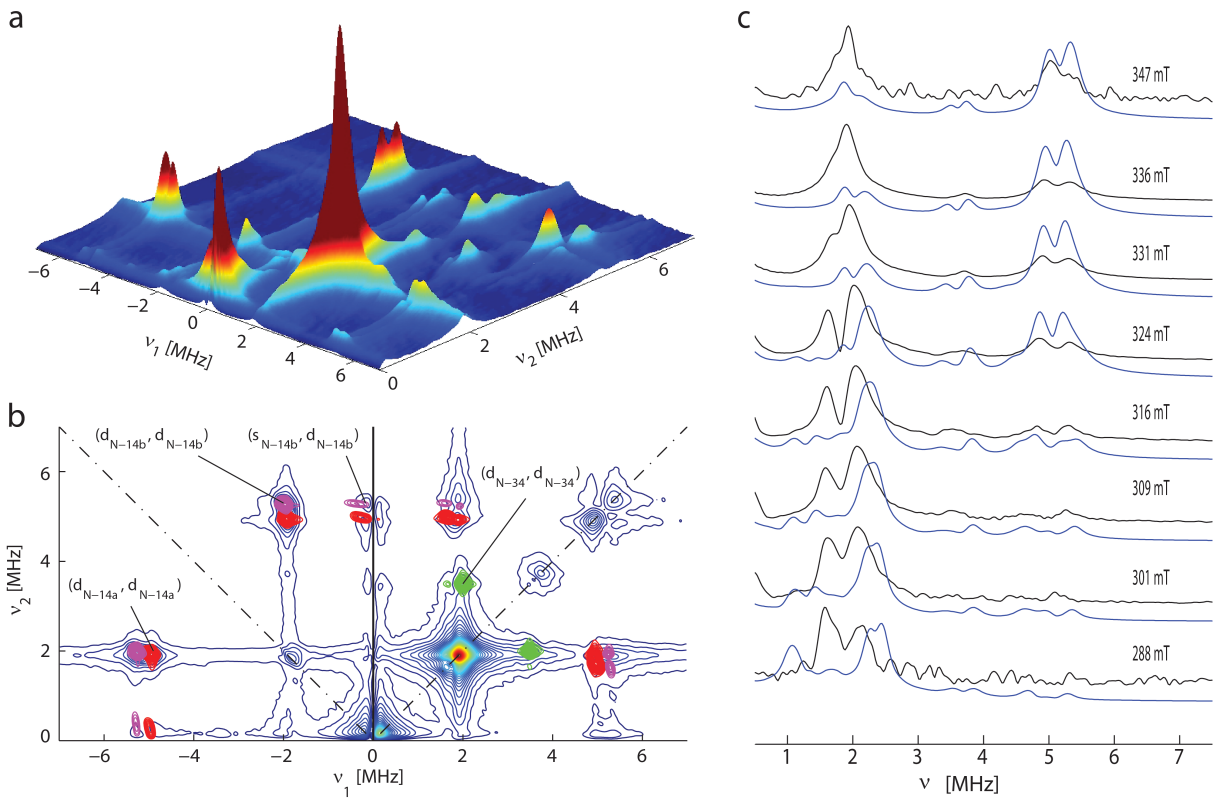

Figure 3. X-band ($\nu = 9.671$ GHz) HYSCORE (335.0 mT) and orientation selective 3-pulse ESEEM spectra of $[Cu^{II}(H_2L^1)(MeOH)_2]^+$ in methanol recorded at 5.0K. (a,b) Surface and contour plots showing the HYSCORE spectrum. (b) A contour plot showing an overlay of the experimental and simulated HYSCORE spectra. ^{14}N single- and double-quantum cross-peaks are labeled 's' and 'd', respectively. A selection of simulated cross-peaks are labeled for three distal ^{14}N atoms (N-14a (red), N-14b (purple) and N-34 (green)). Atom numbers correspond to those given in Figure 5. For reference the nitrogen Larmor frequency is $\nu(^{14}N) = 1.03$ MHz. (c) Orientation selective three-pulse ESEEM spectra (black) recorded at the indicated field positions along with the simulations (blue) for the distal nitrogens. Spin Hamiltonian parameters determined from the simulation of both the HYSCORE and three-pulse ESEEM spectra are given in Table 2.

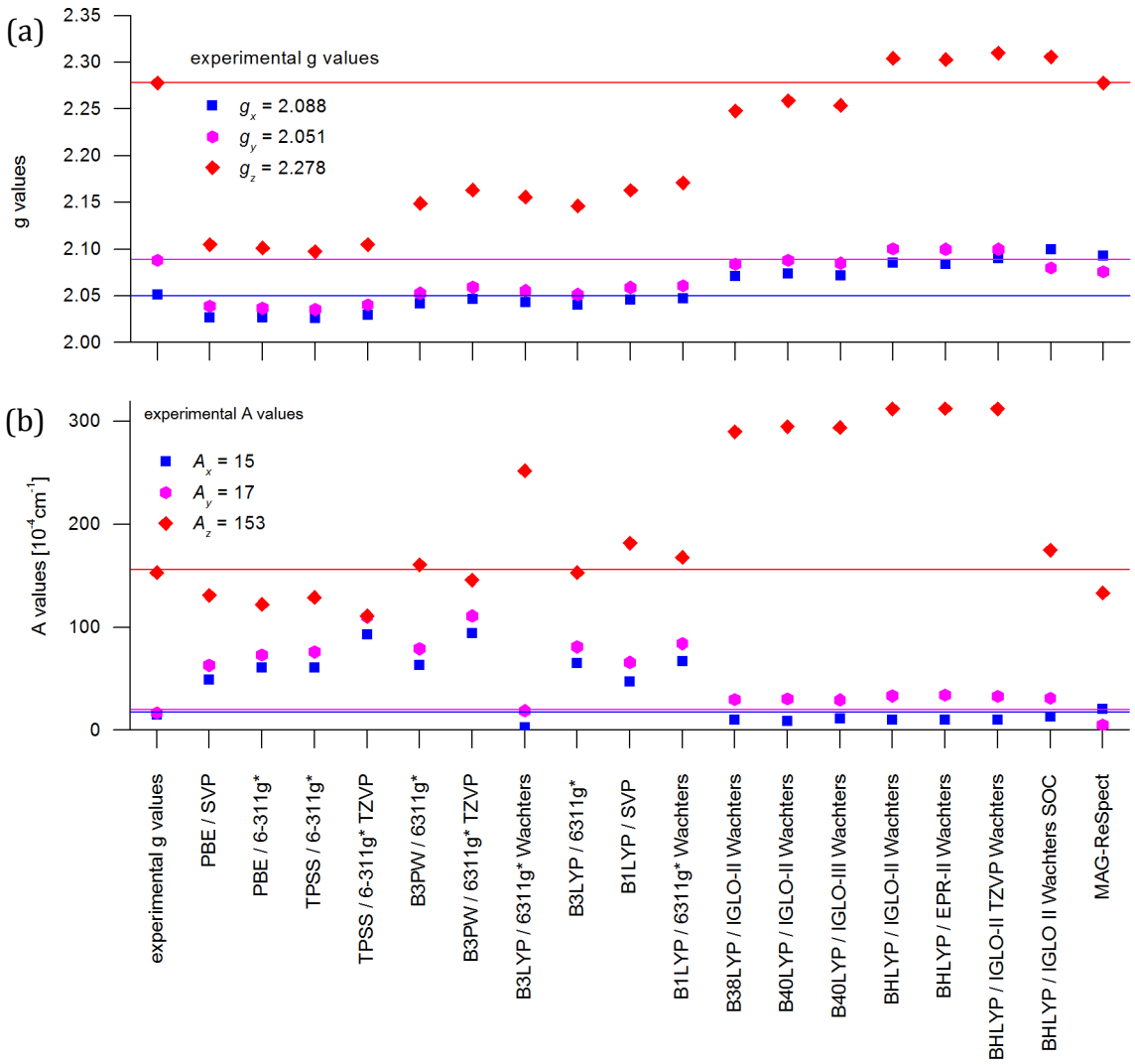

Figure 4. Calculated and experimental (a) g and (b) $|A|$ (^{63}Cu) matrices for $[Cu^{II}(H_2L^1)(MeOH)_2]^+$ calculated with various combinations of functionals and basis sets with the programs ORCA[43] and MAG-ReSpect.[44] The experimental values are depicted as horizontal lines.

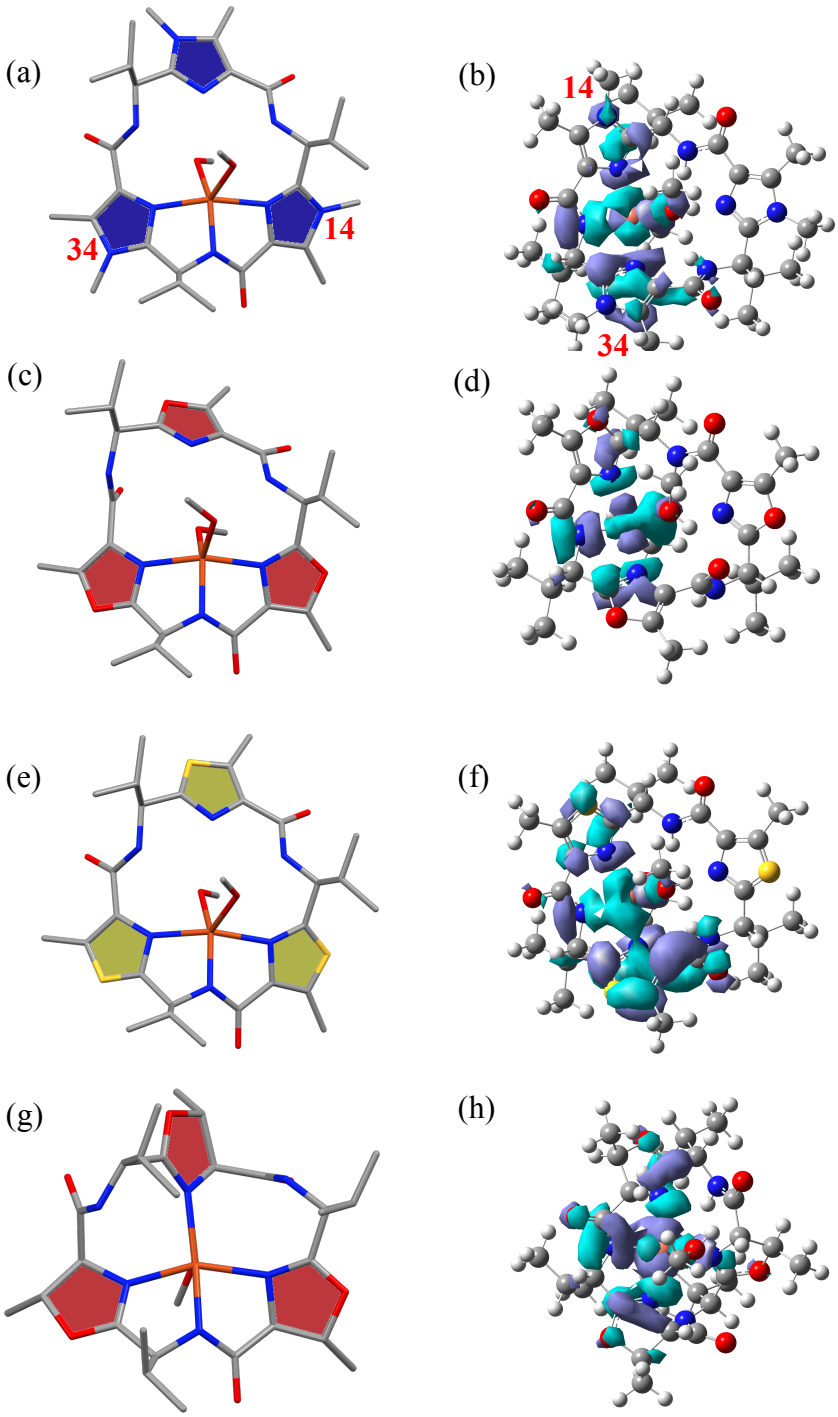

Figure 5. Structures and SOMO's for (a,b) $[Cu^{II}(H_2L^1)(MeOH)_2]^+$, (c,d) $[Cu^{II}(H_2L^2)(MeOH)_2]^+$, (e,f) $[Cu^{II}(H_2L^3)(MeOH)_2]^+$ and (g,h) $[Cu^{II}(H_2L^{wa})(MeOH)_2]^+$ showing delocalization of the unpaired electron onto the N-methylimidazole, thiazole, oxazole and oxazoline rings of the [18]azacrown-6 macrocyclic rings. Nitrogen atom numbers given in red.

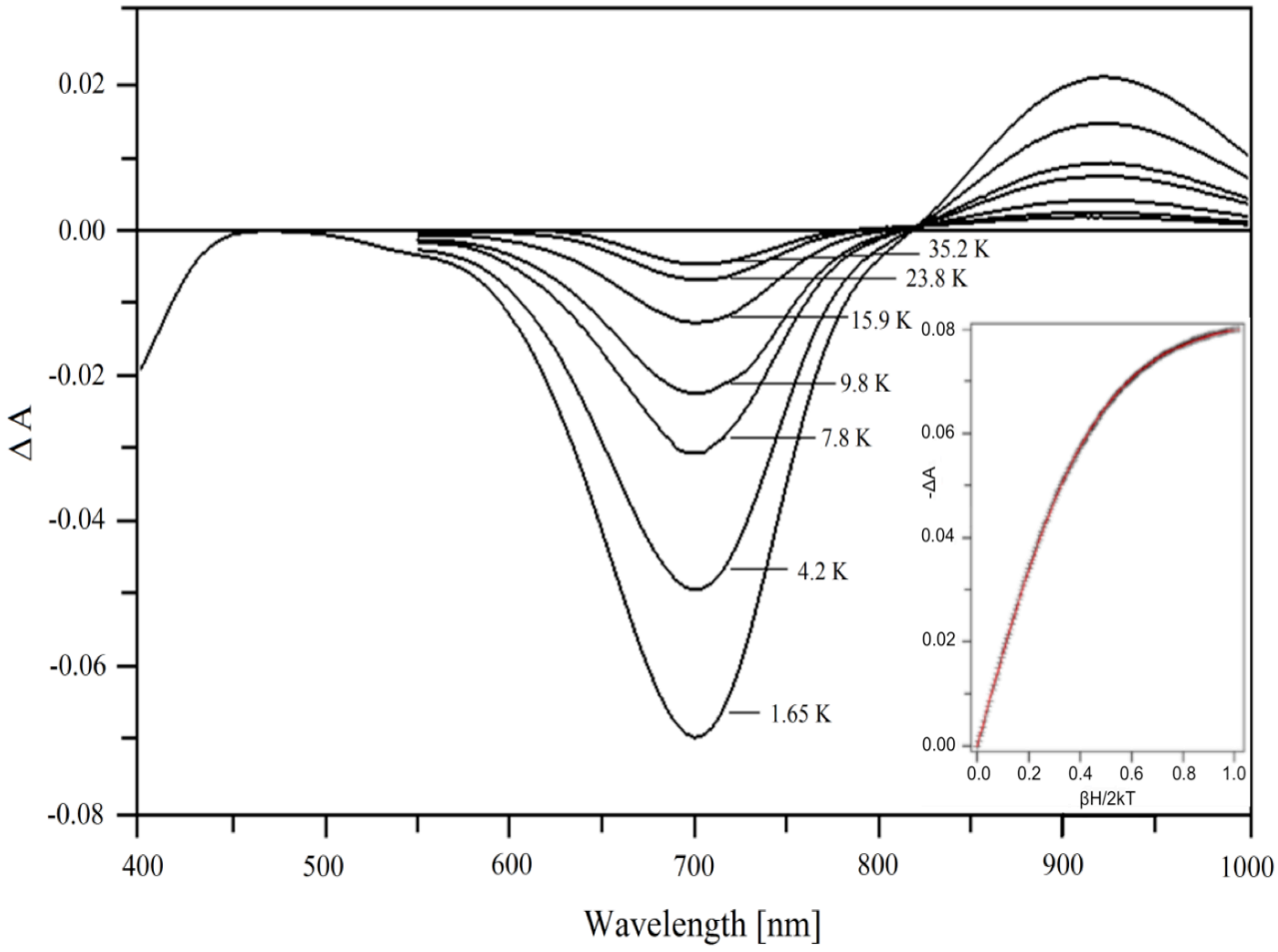

Figure 6. Variable temperature MCD spectra of $[Cu^{II}(H_2L^1)(MeOH)_2]^+$ measured at 5 T in methanol:glycerol (1:1) frozen solution, $c[Cu^{II}(H_2L^1)(MeOH)_2]^+) = 30$ mM. Inset: VTVH saturation curves at $\lambda = 700$ nm, experimental (black crosses) and simulated (red lines). All curves are overlaying.

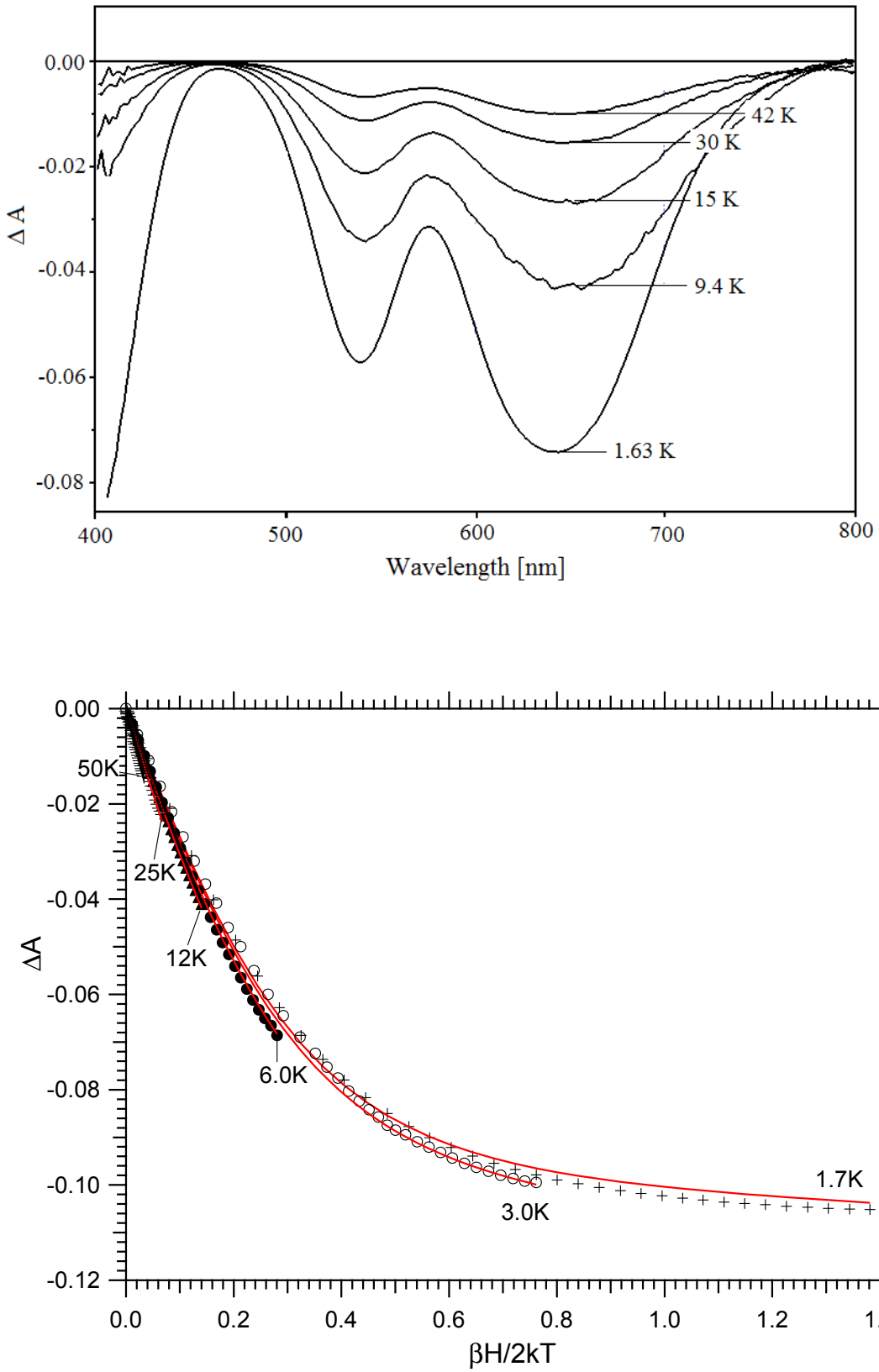

Figure 7. Variable temperature MCD spectra of $[Cu_2^{II}(L^1)(\mu\text{-}OHCH(CH_2OH)_2)]^+$. (a) Experimental spectra measured at 5T in methanol:glycerol (1:1) frozen solution, ($c(H_3L^1)$ = 30 mM), (b) Variable temperature variable field curves (black = experimental, red = fit; λ = 660 nm; T = 1.75 K – 50 K, measured at 7 T. Parameters are given in Table 5.

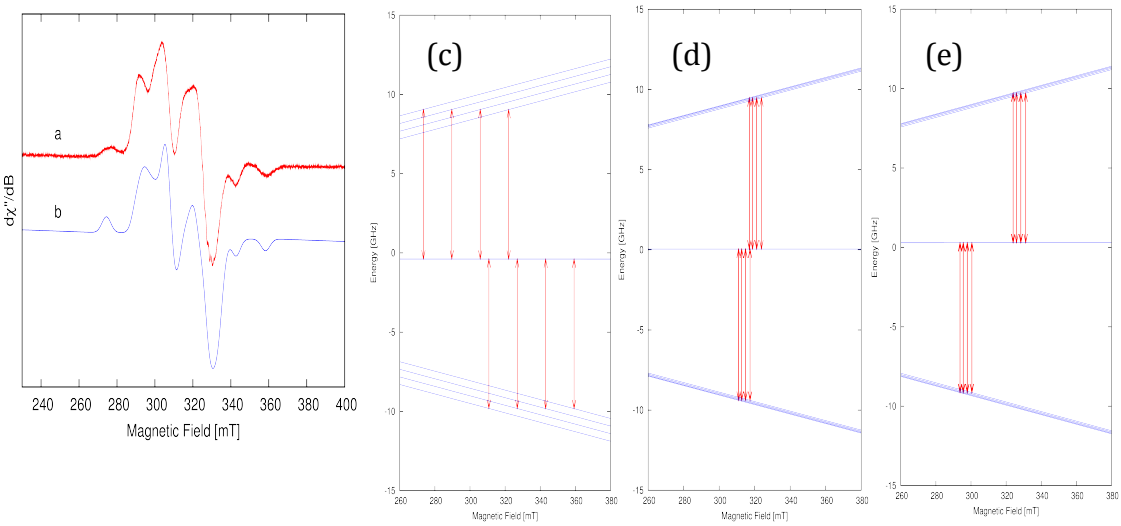

Figure 8. X-Band EPR spectra of $[Cu_2^{II}(L^1)(\mu\text{-}OHCH(CH_2OH)_2)]^+$. (a) Experimental EPR spectrum of $[Cu_2^{II}(L^1)(\mu\text{-}OHCH(CH_2OH)_2)]^+$ in a methanol:glycerol (1:1) frozen solution, $c(H_3L^1)$ = 1.5 mM, ν = 9.434401 GHz, T = 50 K, (b) computer simulation of (a). (c-e) Energy level diagrams showing the allowed EPR transitions along the 'z', 'x' and 'y' principal directions, respectively. Spin Hamiltonian parameters are given in Table 5.

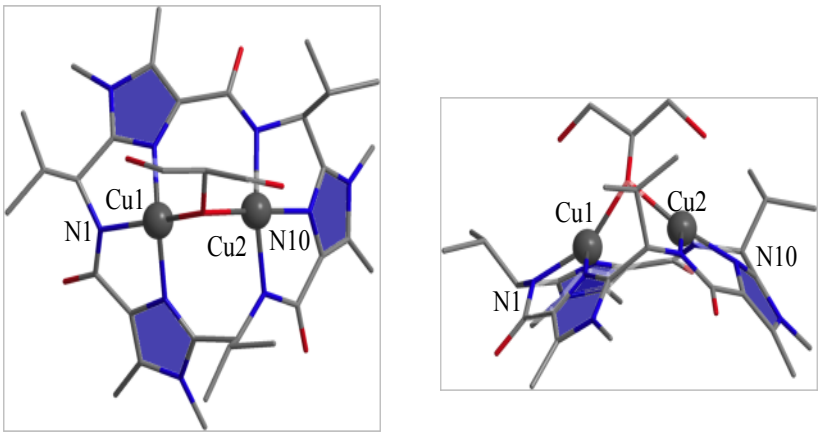

Figure 9. DFT calculated structure (Gaussian03,[40] B3LYP/6-31g*/TZVP) of the glycerol bridged dinuclear Cu^{II} complex $[Cu_2^{II}(L^1)(\mu\text{-}OHCH(CH_2OH)_2]^+$.

Chart 1: Schematic Structures of H_3L^{wa} and H_3L^{1-3}.

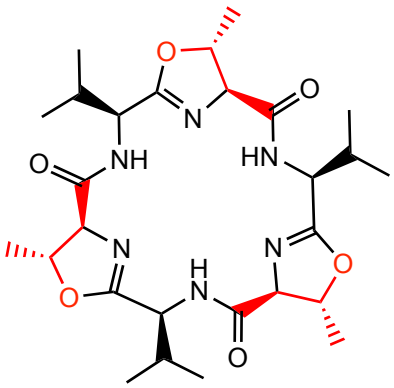

H_3L^{wa}

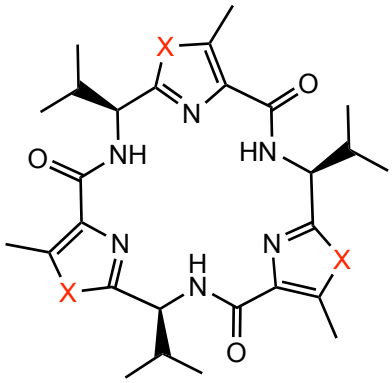

H_3L^1, X = N-CH_3
H_3L^2, X = O
H_3L^3, X = S

Table of Contents Figure

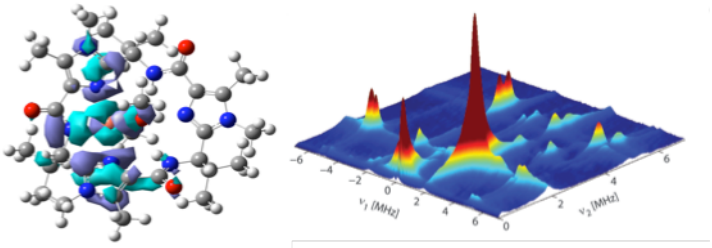

Table of Contents Synopsis

High-resolution orientation selective three-pulse ESEEM, ENDOR and HYSCORE spectroscopy in conjunction with computational chemistry and MCD spectroscopy of $[Cu^{II}(H_2L^1)(MeOH)_2)]^+$ have been utilized to determine the molecular (geometric and electronic) structure of a series of mono- and di-nuclear Cu^{II} complexes of three synthetic analogues of Westiellamide. A systematic exploration of a range of basis sets and DFT functionals was undertaken to determine their ability to reproduce the experimentally determined spin Hamiltonian parameters.